

8

Calorimetry

Most particles end their journey in calorimeters.

Anonymous

Methods of particle energy measurement in modern high energy physics have to cover a large dynamical range of more than 20 orders of magnitude in energy. Detection of extremely small energies (milli-electron-volts) is of great importance in astrophysics if one searches for the remnants of the Big Bang. At the other end of the spectrum, one measures cosmic-ray particles with energies of up to 10^{20} eV, which are presumably of extragalactic origin.

Calorimetric methods imply total absorption of the particle energy in a bulk of material followed by the measurement of the deposited energy. Let us take as an example a 10 GeV muon. Passing through material this particle loses its energy mainly by the ionisation of atoms while other contributions are negligible. To absorb all the energy of the muon one needs about 9 m of iron or about 8 m of lead. It is quite a big bulk of material!

On the other hand, high-energy photons, electrons and hadrons can interact with media producing secondary particles which leads to a shower development. Then the particle energy is deposited in the material much more efficiently. Thus calorimeters are most widely used in high energy physics to detect the electromagnetic and hadronic showers. Accordingly, such detector systems are referred to as *electromagnetic* and *hadron* calorimeters.

At very high energies (≥ 1 TeV), however, also muon calorimetry becomes possible because TeV muons in iron and lead undergo mainly interaction processes where the energy loss is proportional to the muon energy (see Chap. 1), thus allowing muon calorimetry. This technique will become relevant for very high-energy colliders (≥ 1 TeV muon energy).

8.1 Electromagnetic calorimeters

8.1.1 Electron–photon cascades

The dominating interaction processes for spectroscopy in the MeV energy range are the photoelectric and Compton effect for photons and ionisation and excitation for charged particles. At high energies (higher than 100 MeV) electrons lose their energy almost exclusively by bremsstrahlung while photons lose their energy by electron–positron pair production [1] (see Sect. 1.2).

The radiation losses of electrons with energy E can be described by the simplified formula:

$$-\left(\frac{dE}{dx}\right)_{\text{rad}} = \frac{E}{X_0}, \quad (8.1)$$

where X_0 is the radiation length. The probability of electron–positron pair production by photons can be expressed as

$$\frac{dw}{dx} = \frac{1}{\lambda_{\text{prod}}} e^{-x/\lambda_{\text{prod}}}, \quad \lambda_{\text{prod}} = \frac{9}{7}X_0. \quad (8.2)$$

A convenient measure to consider shower development is the distance normalised in radiation lengths, $t = x/X_0$.

The most important properties of electron cascades can be understood in a very simplified model [2, 3]. Let E_0 be the energy of a photon incident on a bulk of material (Fig. 8.1).

After one radiation length the photon produces an e^+e^- pair; electrons and positrons emit after another radiation length one bremsstrahlung photon each, which again are transformed into electron–positron pairs. Let us assume that the energy is symmetrically shared between the particles at

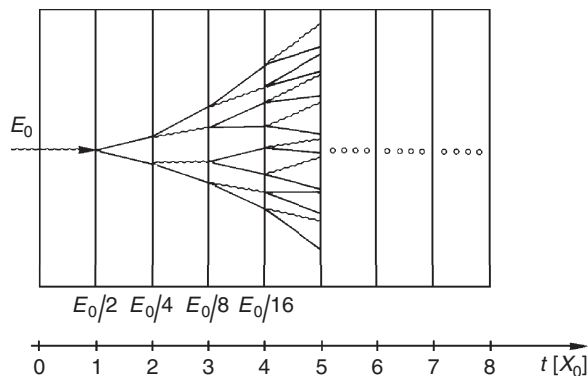


Fig. 8.1. Sketch of a simple model for shower parametrisation.

each step of the multiplication. The number of shower particles (electrons, positrons and photons together) at depth t is

$$N(t) = 2^t, \quad (8.3)$$

where the energy of the individual particles in generation t is given by

$$E(t) = E_0 \cdot 2^{-t}. \quad (8.4)$$

The multiplication of the shower particles continues as long as $E_0/N > E_c$. When the particle energy falls below the critical value E_c , absorption processes like ionisation for electrons and Compton and photoelectric effects for photons start to dominate. The position of the shower maximum is reached at this step of multiplication, i.e. when

$$E_c = E_0 \cdot 2^{-t_{\max}}. \quad (8.5)$$

This leads to

$$t_{\max} = \frac{\ln(E_0/E_c)}{\ln 2} \propto \ln(E_0/E_c). \quad (8.6)$$

Let us take as an example the shower in a CsI crystal detector initiated by a 1 GeV photon. Using the value $E_c \approx 10$ MeV we obtain for the number of particles in the shower maximum $N_{\max} = E_0/E_c = 100$ and for the depth of the shower maximum to be $\approx 6.6 X_0$.

After the shower maximum electrons and positrons* having an energy below the critical value E_c will stop in a layer of $1 X_0$. Photons of the same energy can penetrate a much longer distance. Figure 8.2 presents the energy dependence of the photon interaction length in CsI and lead.

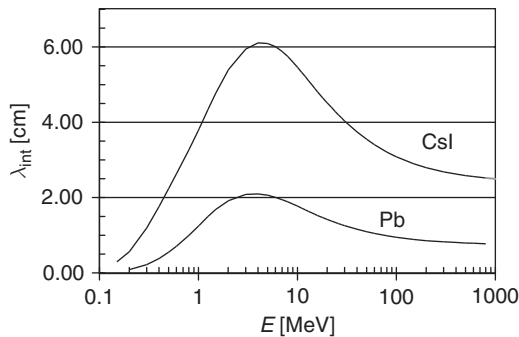


Fig. 8.2. Photon interaction length in lead and CsI [4].

* Throughout this chapter both electrons and positrons are referred to as electrons.

As we can see, this function has a broad maximum between 1 MeV and 10 MeV where it amounts to about $3 X_0$. The energy of photons in the shower maximum close to E_c is just in this range. Thus, to absorb 95% of photons produced in the shower maximum, an additional $7-9 X_0$ of material is necessary which implies that the thickness of a calorimeter with high shower containment should be at least $14-16 X_0$. The energy deposition in an absorber is a result of the ionisation losses of electrons and positrons. Since the $(dE/dx)_{\text{ion}}$ value for relativistic electrons is almost energy-independent, the amount of energy deposited in a thin layer of absorber is proportional to the number of electrons and positrons crossing this layer.

This very simple model already correctly describes the most important qualitative characteristics of *electromagnetic cascades*.

- (i) To absorb most of the energy of the incident photon the total calorimeter thickness should be more than $10-15 X_0$.
- (ii) The position of the shower maximum increases slowly with energy. Hence, the thickness of the calorimeter should increase as the logarithm of the energy but not proportionally as for muons.
- (iii) The energy leakage is caused mostly by soft photons escaping the calorimeter at the sides (lateral leakage) or at the back (rear leakage).

In reality the shower development is much more complicated. This is sketched in Fig. 8.3. An accurate description of the shower development is

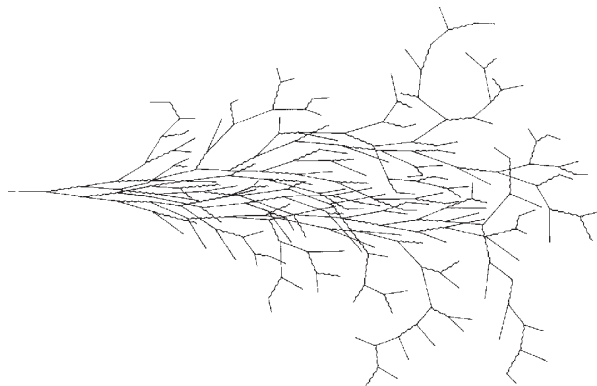


Fig. 8.3. Schematic representation of an electromagnetic cascade. The wavy lines are photons and the solid lines electrons or positrons.

a difficult task. Earlier, large efforts were undertaken to develop an analytical approach [5]. At present, due to the increase of the computer capacity, an accurate description is obtained from Monte Carlo simulations.

The longitudinal distribution of the energy deposition in electromagnetic cascades is reasonably described by an approximation based on the Monte Carlo programme EGS [6, 7],

$$\frac{dE}{dt} = E_0 b \frac{(bt)^{a-1} e^{-bt}}{\Gamma(a)} , \quad (8.7)$$

where $\Gamma(a)$ is Euler's Γ function, defined by

$$\Gamma(g) = \int_0^\infty e^{-x} x^{g-1} dx . \quad (8.8)$$

The gamma function has the property

$$\Gamma(g + 1) = g \Gamma(g) . \quad (8.9)$$

Here a and b are model parameters and E_0 is the energy of the incident particle. In this approximation the maximum of the shower development is reached at

$$t_{\max} = \frac{a - 1}{b} = \ln \left(\frac{E_0}{E_c} \right) + C_{\gamma e} , \quad (8.10)$$

where $C_{\gamma e} = 0.5$ for a gamma-induced shower and $C_{\gamma e} = -0.5$ for an incident electron. The parameter b as obtained from simulation results is $b \approx 0.5$ for heavy absorbers from iron to lead. Then the energy-dependent parameter a can be derived from Eq. (8.10).

The experimentally measured distributions [8–10] are well described by a Monte Carlo simulation with the code EGS4 [1, 6]. Formula (8.7) provides a reasonable approximation for electrons and photons with energies larger than 1 GeV and a shower depth of more than $2 X_0$, while for other conditions it gives a rough estimate only. The *longitudinal development of electron cascades* in matter is shown in Figs. 8.4 and 8.5 for various incident energies. The distributions are slightly dependent on the material (even if the depth is measured in units of X_0) due to different E_c , as shown in Fig. 8.4, bottom.

The angular distribution of the produced particles by bremsstrahlung and pair production is very narrow (see Chap. 1). The characteristic angles are on the order of $m_e c^2 / E_\gamma$. That is why the *lateral width of an electromagnetic cascade* is mainly determined by multiple scattering and can be best characterised by the *Molière radius*

$$R_M = \frac{21 \text{ MeV}}{E_c} X_0 \{ \text{g/cm}^2 \} . \quad (8.11)$$

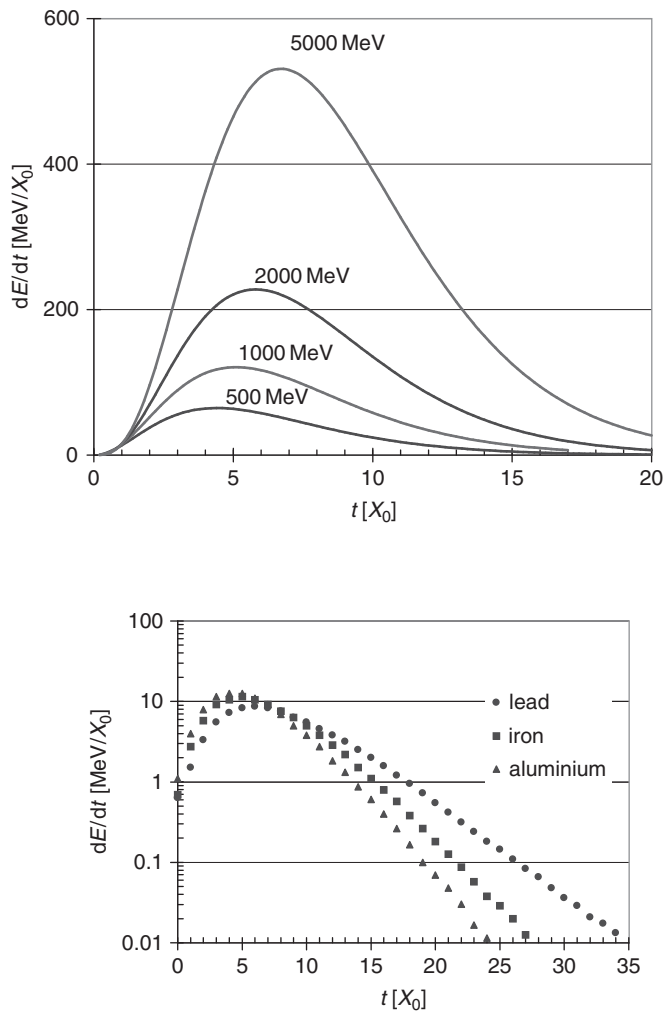


Fig. 8.4. Longitudinal shower development of electromagnetic cascades. Top: approximation by Formula (8.7). Bottom: Monte Carlo simulation with EGS4 for 10 GeV electron showers in aluminium, iron and lead [11].

Figure 8.6 shows the longitudinal and lateral development of a 6 GeV electron cascade in a lead calorimeter (based on [12, 13]). The lateral width of an electromagnetic shower increases with increasing longitudinal shower depth. The largest part of the energy is deposited in a relatively narrow shower core. Generally speaking, about 95% of the shower energy is contained in a cylinder around the shower axis whose radius is $R(95\%) = 2R_M$ almost independently of the energy of the incident particle. The dependence of the containment radius on the material is taken into account by the critical energy and radiation length appearing in Eq. (8.11).

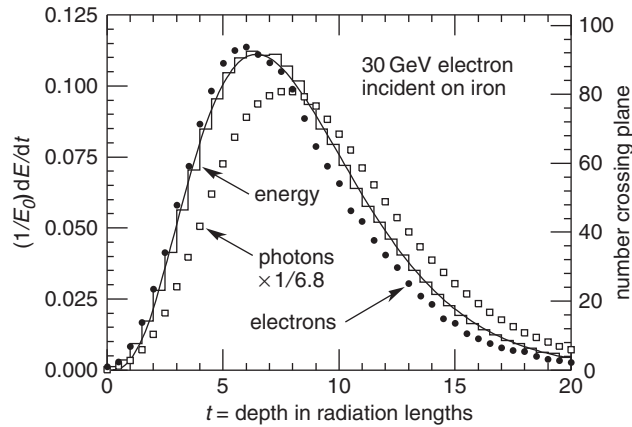


Fig. 8.5. Longitudinal shower development of a 30 GeV electron-induced cascade obtained by the EGS4 simulation in iron [1, 6]. The solid histogram shows the energy deposition; black circles and open squares represent the number of electrons and photons, respectively, with energy larger than 1.5 MeV; the solid line is the approximation given by (8.7).

Another important shower characteristic is the number of electrons and photons crossing a plane at a certain shower depth. A simple estimation of the electron number N_e can be done taking into account that the energy deposition in a shower is provided by the ionisation losses of the charged particle and

$$\left(\frac{dE}{dx}\right)_{\text{ion}} \cdot X_0 = E_c \quad (8.12)$$

Then one can estimate

$$N_e(t) = \frac{1}{E_c} \frac{dE}{dt} \quad (8.13)$$

However, a considerable part of the shower particles is soft. Since only electrons above a certain threshold are detected, the effective number of shower particles becomes much smaller. Figure 8.5 shows the numbers of electrons and photons with energy above 1.5 MeV as well as dE/dt values for a 30 GeV shower in iron [1]. We can see that N_e in this case is about a factor of two lower than given by Formula (8.13).

At very high energies the development of electromagnetic cascades in dense media is influenced by the *Landau-Pomeranchuk-Migdal (LPM) effect* [14, 15]. This effect predicts that the production of low-energy photons by high-energy electrons is suppressed in dense media. When an electron interacts with a nucleus producing a bremsstrahlung photon the longitudinal momentum transfer between the electron and nucleus is very

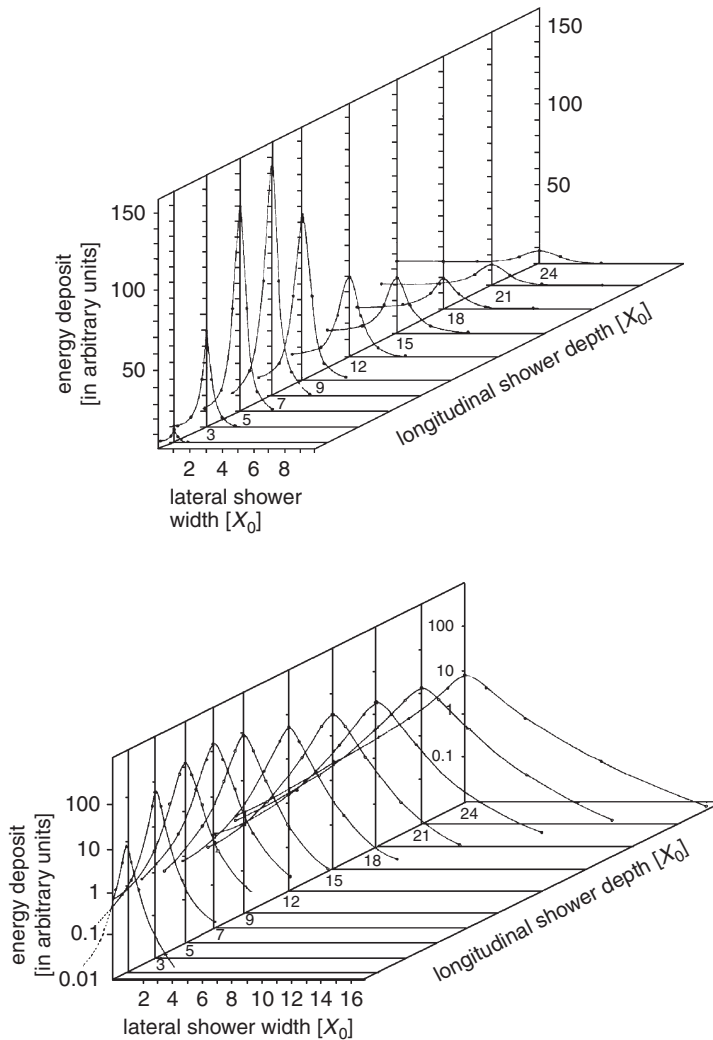


Fig. 8.6. Longitudinal and lateral development of an electron shower (6 GeV) in lead shown in linear and logarithmic scales (based on [12, 13]).

small. Heisenberg's uncertainty principle therefore requires that the interaction must take place over a long distance, which is called the *formation zone*. If the electron is disturbed while travelling this distance, the photon emission can be disrupted. This can occur for very dense media, where the distance between scattering centres is small compared to the spatial extent of the wave function. The Landau–Pomeranchuk–Migdal effect predicts that in dense media multiple scattering of electrons is sufficient to suppress photon production at the low-energy end of the bremsstrahlung

spectrum. The validity of this effect has been demonstrated by an experiment at SLAC with 25 GeV electrons on various targets. The magnitude of the photon suppression is consistent with the LPM prediction [16, 17].

The LPM effect is relevant for experiments with ultrahigh-energy cosmic rays and should be taken into account for the design of calorimeters at high-energy accelerators and storage rings such as the LHC.

8.1.2 Homogeneous calorimeters

Homogeneous calorimeters are constructed from a material combining the properties of an absorber and a detector. It means that practically the total volume of the calorimeter is sensitive to the deposited energy. These calorimeters are based on the measurement of the scintillation light (scintillation crystals, liquid noble gases), ionisation (liquid noble gases) and the Cherenkov light (lead glass or heavy transparent crystals).

The main parameters of electromagnetic calorimeters are the energy and position resolution for photons and electrons. The energy resolution σ_E/E is determined both by physical factors like the fluctuation of the energy leakage or photoelectron statistics and technical ones like non-uniformity of crystals.

For all calorimeter types the common contribution to the energy resolution originates from fluctuations of the energy leakage and from fluctuations of the first interaction point. The energy resolution can be expressed as

$$\sigma_{\text{int}}^2 = \sigma_1^2 + \sigma_r^2 + \sigma_l^2 + \sigma_b^2, \quad (8.14)$$

where σ_1 is determined by the fluctuations of the point of the first interaction, σ_r is the rear leakage, σ_l the lateral leakage and σ_b the leakage due to albedo fluctuations. The average photon path in the material before the first conversion is $9/7 X_0$ with a spread of roughly $1 X_0$. The spread implies that the effective calorimeter thickness changes event by event. Looking at the transition curve of Fig. 8.6 we can estimate σ_1 as

$$\sigma_1 \approx \left(\frac{dE}{dt} \right)_{t=t_{\text{cal}}} X_0, \quad (8.15)$$

where t_{cal} is the total calorimeter thickness. It is clear that σ_1 is getting larger with increasing energy.

As discussed earlier, the energy leakage is mostly due to low-energy (1–10 MeV) photons. The albedo is usually quite small ($< 1\%$ of the initial energy) and the induced contribution to the energy resolution is negligible. At first glance the lateral size of the calorimeter should be chosen as large as necessary to make the lateral energy leakage negligible. But in a real experiment, where an event contains several or many particles, a lateral

size of the area assigned to a certain particle should be limited by a few R_M . The fraction of lateral energy leakage is practically independent of the photon energy. Even though the number of escaping photons increases with the photon energy, the relative fluctuations σ_1/E_0 should go down.

The value of σ_r/E_0 has a slow energy dependence. Often the terms σ_1 and σ_r are considered combined. A detailed review of the physics of shower development and fluctuations can be found in the book by Wigmans [11].

Crystal calorimeters are based on heavy scintillation crystals (see Sect. 5.4, Table 5.2). These detectors are usually built as hodoscopes with a transverse size of elements of order one to two R_M . Then the shower energy is deposited in a group of crystals usually referred to as *cluster*. The light readout is performed by photomultiplier tubes, vacuum phototriodes or silicon photodiodes (see Sect. 5.5). One of the calorimeters of this kind is described in Chap. 13. At present the best energy resolutions are obtained with calorimeters of this type [18–22].

A typical energy spectrum measured in a calorimeter is shown in Fig. 8.7 [23]. For a high-resolution detector system it is usually asymmetric, with a rather long ‘tail’ to lower energies, and the energy resolution is conventionally parametrised as

$$\sigma_E = \frac{\text{FWHM}}{2.35} . \quad (8.16)$$

This asymmetric distribution can be approximated, for example, by the logarithmic Gaussian shape

$$dW = \exp \left\{ -\frac{\ln^2[1 - \eta(E - E_p)/\sigma]}{2s_0^2} - \frac{s_0^2}{2} \right\} \frac{\eta dE}{\sqrt{2\pi}\sigma s_0} , \quad (8.17)$$

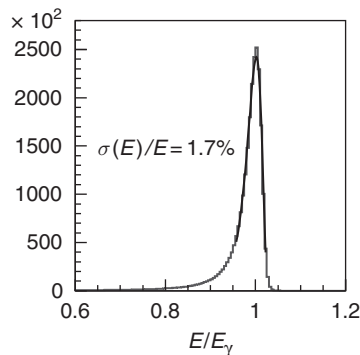


Fig. 8.7. Typical energy spectrum measured in a calorimeter [23] for photons of 4–7 GeV. The solid line is the approximation by Formula (8.17).

where E_p is the energy corresponding to the peak, $\sigma = \text{FWHM}/2.35$, η the asymmetry parameter and s_0 can be written as

$$s_0 = \frac{2}{\xi} \operatorname{arsinh} \left(\frac{\eta \xi}{2} \right), \quad \xi = 2.35. \quad (8.18)$$

When $\eta \rightarrow 0$, the distribution becomes Gaussian.

Various approximations were used to describe the energy dependence of the resolution of calorimeters. Figure 8.8 shows the energy resolution of a calorimeter made of $16 X_0$ CsI crystals for photons in the range from 20 MeV to 5.4 GeV [24]. The light readout was done with two 2 cm^2 photodiodes per crystal. The energy resolution was approximated as

$$\frac{\sigma_E}{E} = \sqrt{\left(\frac{0.066\%}{E_n} \right)^2 + \left(\frac{0.81\%}{\sqrt[4]{E_n}} \right)^2 + (1.34\%)^2}, \quad E_n = E/\text{GeV}, \quad (8.19)$$

where the term proportional to $1/E$ stands for the electronics-noise contribution.

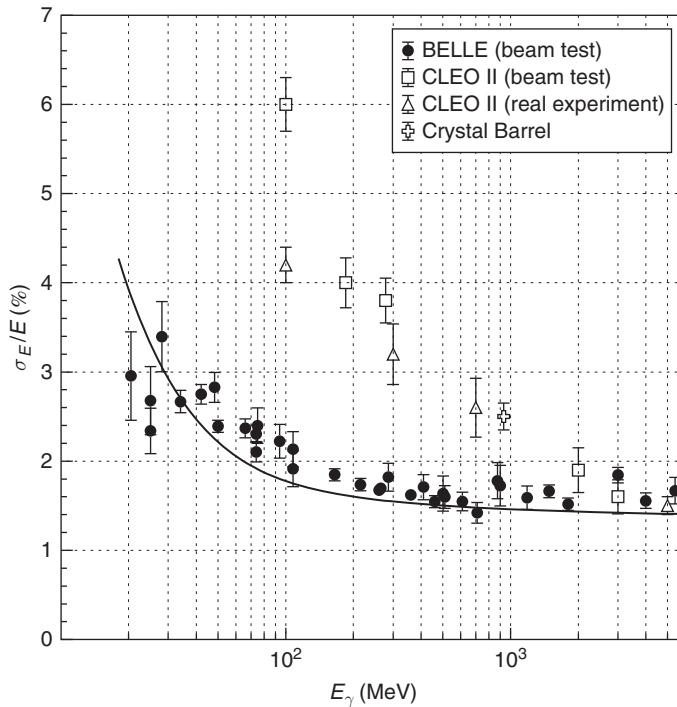


Fig. 8.8. The energy resolution as a function of the incident-photon energy [24]. The solid line is the result of an MC simulation. For the Belle data a cluster of 5×5 crystals at a threshold of 0.5 MeV was used.

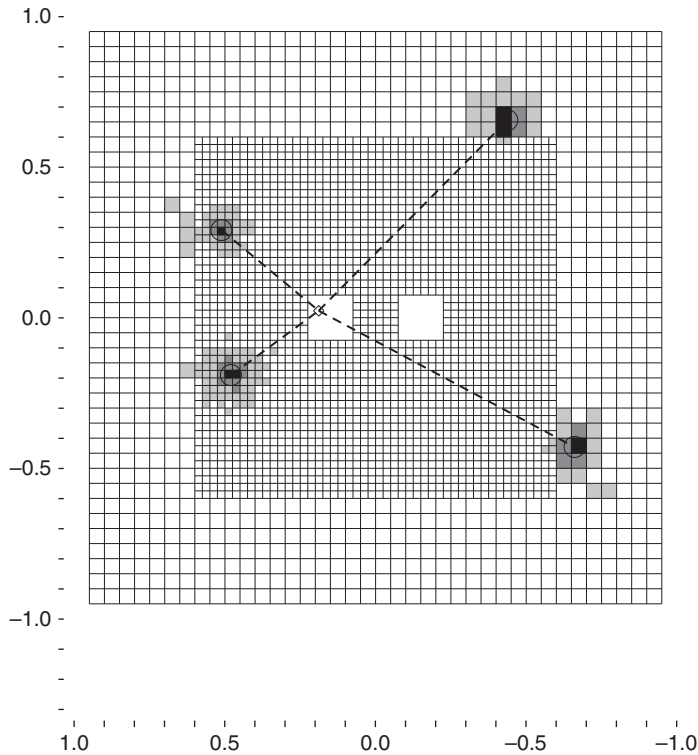


Fig. 8.9. A view of the clusters in the KTeV calorimeter for a typical event of a $K_L \rightarrow \pi^0 \pi^0$ decay [22]. The calorimeter modules have a cross section of $5 \times 5 \text{ cm}^2$ ($2.5 \times 2.5 \text{ cm}^2$) in the outer (inner) part. The hit crystals are shaded.

In discussing crystal calorimeters for high energies we have to mention the one for the KTeV experiment that was based on about 3200 pure CsI crystals of 50 cm ($27 X_0$) length [22]. This device was intended for the detection of photons with energies up to 80 GeV, and an impressive energy resolution σ_E/E better than 1% for energies larger than 5 GeV was achieved. Figure 8.9 presents a view of the energy clusters in this calorimeter for a typical event of a $K_L \rightarrow \pi^0 \pi^0$ decay. All photons are clearly separated.

At present the most sophisticated project of a calorimeter of this type is under development for the Compact Muon Solenoid (CMS) detector [25] at the CERN LHC proton–proton collider. The CMS electromagnetic calorimeter [26] incorporates 80 000 lead-tungstate (PbWO_4 or PWO) crystals mounted with other CMS subdetectors including the hadron calorimeter inside the superconducting solenoid, which produces a 4 T magnetic field. These crystals (see Table 5.2) have been chosen as a detector medium due to their short radiation length (0.89 cm), small Molière

radius (2.19 cm), fast scintillation emission and high radiation hardness. However, the relatively low light output, ≈ 50 photons/MeV for full-size crystals, imposes hard constraints on the readout scheme. The crystal size is $22 \times 22 \times 230 \text{ mm}^3$ ($1 R_M \times 1 R_M \times 26 X_0$) for the barrel and $30 \times 30 \times 220 \text{ mm}^3$ for the endcaps. The light readout in the barrel part is performed by two $5 \times 5 \text{ mm}^2$ avalanche photodiodes (APDs). The APDs were chosen for readout because in addition to their intrinsic gain (in CMS a gain of 50 is used) APDs are compact and insensitive to magnetic fields; they also show a low nuclear counter effect and exhibit a high radiation resistance. For CMS a special optimised device has been developed [27]. Since the radiation background in the endcaps is much higher than that in the barrel, a vacuum phototriode (VPT) was chosen as photodetector for the endcap modules.

The energy resolution of the CMS electromagnetic calorimeter can be approximated as

$$\frac{\sigma_E}{E} = \frac{a}{\sqrt{E}} \oplus \frac{b}{E} \oplus c, \quad (8.20)$$

where a stands for photoelectron statistics (sometimes called stochastic term), b for the electronics noise, and c appears due to the calibration uncertainty and crystal non-uniformity (the symbol \oplus means summation in quadrature). The design goals for the barrel (endcap) are $a = 2.7\%$ (5.7%), $b = 155 \text{ MeV}$ (205 MeV), $c = 0.55\%$ (0.55%). This was confirmed by tests with a prototype [28].

A disadvantage of crystal calorimeters is the high cost of the scintillation crystals and limitations in the production of large volumes of this material. To circumvent these constraints, *lead-glass blocks* can be used in homogeneous calorimeters instead of crystals. The properties of typical lead glass (Schott SF-5 or Corning CEREN 25) are: density of about 4 g/cm^3 , radiation length of $X_0 \approx 2.5 \text{ cm}$ and refractive index of $n \approx 1.7$. The Cherenkov-radiation threshold energy for electrons in this glass is quite low, $T_{\text{ct}}^e \approx 120 \text{ keV}$ implying that the total number of Cherenkov photons is proportional to the total track length of all charged particles in a shower developing in the lead-glass absorber. Since the energy deposition in the electron–photon shower is provided by the ionisation losses of electrons, which is also proportional to the total track length, one can assume that the total number of Cherenkov photons is proportional to the deposited energy.

However, the amount of Cherenkov light is much less (by, roughly, a factor of 1000) compared to that of conventional scintillators. This results in a large contribution of photoelectron statistics to the energy resolution of *lead-glass calorimeters*. The OPAL experiment at CERN [29], which used lead glass for the endcap calorimeter, reported an energy resolution of

$$\frac{\sigma_E}{E} = \frac{5\%}{\sqrt{E[\text{GeV}]}} , \quad (8.21)$$

dominated by the stochastic term. Recently, the SELEX experiment at Fermilab demonstrated a high performance of its lead-glass calorimeter [30]. However, it should be noted that at present homogeneous Cherenkov calorimeters are becoming quite rare. The main reason probably is the progress in sampling calorimeters (discussed later), which achieve now the same range of energy resolution.

Homogeneous *ionisation calorimeters* can be built as an array of ionisation chambers immersed into liquid xenon [31, 32] or liquid krypton [33, 34] (see also Sect. 5.2). The energy resolution achieved with calorimeters of this type is close to that for crystal detectors. The NA48 experiment approximates the energy resolution of its LKr calorimeter [33] by Formula (8.20) with a set of the following parameters:

$$a = 3.2\% , \quad b = 9\% , \quad c = 0.42\% . \quad (8.22)$$

This device is intended as a photon detector in the 10–100 GeV energy range. One more example is the LKr calorimeter of the KEDR detector [32]. The energy resolution obtained with a prototype is described by the same formula with $a = 0.3\%$, $b = 1.6\%$, $c = 1.6\%$ [35].

The initial layers of the LXe or LKr calorimeters can be designed as a series of fine-grained strips or wire ionisation chambers. Then the lateral position of the photon conversion point can be measured with high accuracy. For example, in [35] the photon spatial resolution was measured to be about $\sigma_r \approx 1$ mm, almost independent of the photon energy.

In calorimeters without longitudinal segmentation the photon angles (or coordinates) are measured usually as corrected centre of gravity of the energy deposition,

$$\theta_\gamma = \frac{\sum \theta_i E_i}{\sum E_i} F_\theta(\varphi, \theta, E) , \quad \varphi_\gamma = \frac{\sum \varphi_i E_i}{\sum E_i} F_\varphi(\varphi, \theta, E) , \quad (8.23)$$

where E_i , θ_i , φ_i are, respectively, the energy deposited in the i th calorimeter element with the angular coordinates θ_i and φ_i . The correction functions (F) can be usually written as a product of functions containing only one of the angles and the energy. The angular resolution depends on the energy and the calorimeter granularity. A general limitation is due to the finite number of particles in a shower. Since the shower cross section is almost energy-independent, the uncertainty in the lateral shower position can be roughly estimated as

$$\sigma_{lp} = \frac{R_M}{\sqrt{N_{\text{tot}}}} = \frac{R_M}{\sqrt{E/E_c}} , \quad (8.24)$$

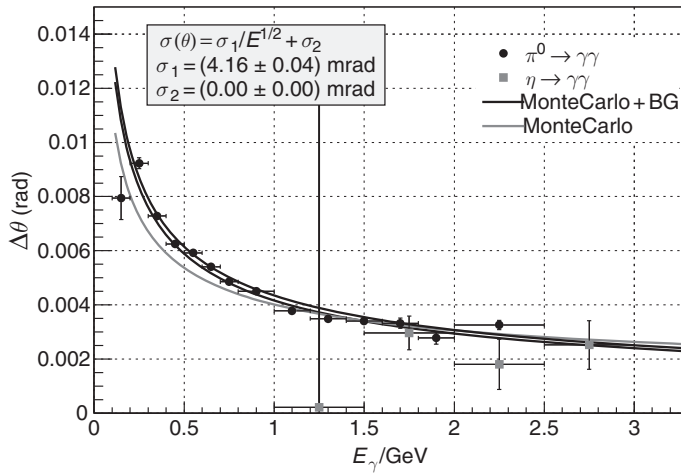


Fig. 8.10. Angular resolution of the calorimeter of the BaBar detector. The lower curve is a Monte Carlo simulation, and the upper one includes background (BG). The central line is a fit to the data, where the fit parameters are given in the inset [20].

where E_c is the critical energy. This leads to $\sigma_{1p} \approx 4$ mm for $E_\gamma = 1$ GeV and a CsI crystal. This is in surprisingly good agreement with the experimental results. A typical energy dependence of the angular resolution (obtained by the BaBar detector [20]) is presented in Fig. 8.10. The energy dependence is parametrised by

$$\sigma(\theta) = \frac{4.2 \text{ mrad}}{\sqrt{E [\text{GeV}]}}, \quad (8.25)$$

8.1.3 Sampling calorimeters

There is a simpler and more economical way to measure the photon energy if the ultimate energy resolution is not crucial. Let us look again at the simplest shower model and place a thin flat counter behind a thick layer of an absorber corresponding to the depth of the shower maximum. In this naïve model the number of electrons crossing the counter, see Formulae (8.5) and (8.6), is just $2/3$ of $N_{\text{max}} = E_\gamma/E_c$, because N_{max} is equally shared between electrons, positrons and photons. The amplitude of the counter signal is normally proportional to the number of charged particles. For a lead absorber ($E_c = 7.4$ MeV) and $E_\gamma = 1$ GeV, one gets $N_e \approx 90$. The relative fluctuation of this value is

$$\frac{\sigma(N_e)}{N_e} = \frac{1}{\sqrt{N_e}} \approx 10\% ; \quad (8.26)$$

that provides not so bad an energy resolution! Of course, the real pattern of the shower development is much more complicated (see Figs. 8.3 and 8.4). In a realistic model the number of electrons crossing the plane at a certain depth is much smaller than that expected from Formula (8.26).

To take advantage of the discussed idea one normally designs a calorimeter as an array of thin counters separated by layers of absorbers. These types of calorimeters are referred to as *sampling calorimeters* since only a sample of the energy deposition is measured. In addition to the general energy-leakage fluctuation the energy resolution of these calorimeters is affected by sampling fluctuations.

If the energy is determined by detectors in which only track segments of shower particles are registered, the number of intersection points with the detector layers is given by

$$N_{\text{tot}} = \frac{T}{d} , \quad (8.27)$$

where T is the total track length and d is the thickness of one sampling layer (absorber plus detector). The value of T can be estimated just as $T = (E_\gamma/E_c) \cdot X_0$, see Eq. (8.12). For the example considered above and $d = 1 X_0$ we get $N_{\text{tot}} \approx 135$ and the sampling fluctuations are $1/\sqrt{N_{\text{tot}}} \approx 8.6\%$.

Actually, as discussed earlier, the number of detected particles is strongly dependent on the detection threshold. The measurable track length can be parametrised by [36]

$$T_m = F(\xi) \cdot \frac{E_\gamma}{E_c} \cdot X_0 \{ \text{g/cm}^2 \} , \quad (8.28)$$

where $T_m \leq T$ and the parameter ξ is a function of the detection energy threshold ϵ_{th} . However, the $\xi(\epsilon_{\text{th}})$ dependence is not very pronounced if ϵ_{th} is chosen to be sufficiently small ($\approx \text{MeV}$). The function $F(\xi)$ takes into account the effect of the cutoff parameter on the total measurable track length for completely contained electromagnetic cascades in a calorimeter. $F(\xi)$ can be parametrised as [36]

$$F(\xi) = [1 + \xi \ln(\xi/1.53)] e^\xi , \quad (8.29)$$

where

$$\xi = 2.29 \cdot \frac{\epsilon_{\text{th}}}{E_c} . \quad (8.30)$$

Using the measurable track length defined by Eq. (8.28), the number of track segments is then

$$N = F(\xi) \cdot \frac{E_\gamma}{E_c} \cdot \frac{X_0}{d} . \quad (8.31)$$

Here we neglected the fact that, because of multiple scattering, the shower particles have a certain angle θ with respect to the shower axis. The effective sampling thickness is therefore not d , but rather $d/\cos\theta$. However, the average value $\langle 1/\cos\theta \rangle$ is not large; it is in the range between 1 and 1.3 depending on the energy E_γ .

Using Poisson statistics the sampling fluctuations limit the energy resolution to

$$\left[\frac{\sigma(E_\gamma)}{E_\gamma} \right]_{\text{samp}} = \sqrt{\frac{E_c \cdot d}{F(\xi) \cdot E_\gamma \cdot X_0 \cdot \cos\theta}} \quad (8.32)$$

As can be seen from Eq. (8.32), the energy resolution of a sampling calorimeter for a fixed given material improves with $\sqrt{d/E_\gamma}$. However, Formula (8.32) does not take into account the correlations which are induced by electrons penetrating through two or several counter planes. These correlations become quite important when $d \ll 1 X_0$ and limit the improvement of the resolution at small d .

A more accurate and simpler expression is suggested in [11] for the *sampling fluctuations* of calorimeters with counters based on condensed material:

$$\frac{\sigma_{\text{samp}}}{E} = \frac{2.7\%}{\sqrt{E [\text{GeV}]}} \sqrt{\frac{s [\text{mm}]}{f_{\text{samp}}}} \quad (8.33)$$

Here s is the thickness of the sensitive layer and f_{samp} is the so-called *sampling fraction*, which is the ratio of ionisation losses of minimum-ionising particles in the sensitive layer to the sum of the losses in the sensitive layer and absorber. Figure 8.11 presents the energy resolution of some calorimeters versus the value $\sqrt{s/f_{\text{samp}}}$ [11]. Anyway, these empirical formulae are only used for a preliminary estimate and general understanding of the sampling-calorimeter characteristics, while the final parameters are evaluated by a Monte Carlo simulation.

As sensitive elements of sampling calorimeters, gas-filled chambers, liquid-argon ionisation detectors, ‘warm’ liquids (e.g. TMS) and scintillators are used. Energy depositions from large energy transfers in ionisation processes can further deteriorate the energy resolution. These Landau fluctuations are of particular importance for thin detector layers. If δ is the average energy loss per detector layer, the Landau fluctuations of the ionisation loss yield a contribution to the energy resolution of [36, 37]

$$\left[\frac{\sigma(E)}{E} \right]_{\text{Landau fluctuations}} \propto \frac{1}{\sqrt{N} \ln(k \cdot \delta)} \quad (8.34)$$

where k is a constant and δ is proportional to the matter density per detector layer.

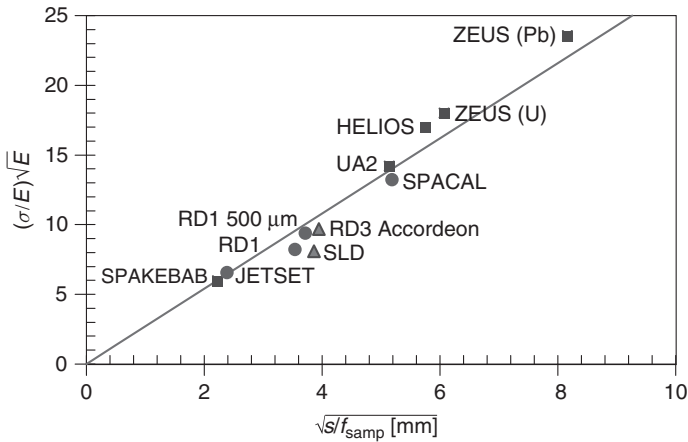


Fig. 8.11. The energy resolution of some sampling calorimeters. The solid line is approximation (8.33) [11]. (The energy is measured in GeV and the ordinate values are given in per cent.)

Since fluctuations of the ionisation losses are much higher in gases than in dense materials, the energy resolution for calorimeters with gaseous counters ($\sigma_E/E \approx 5\%–20\%$ at 1 GeV) is worse compared to that for liquid argon or scintillator sampling.

In *streamer-tube calorimeters* tracks are essentially counted, at least as long as the particles are not incident under too large an angle with respect to the shower axis, which is assumed to be perpendicular to the detector planes. For each ionisation track exactly one streamer is formed – independent of the ionisation produced along the track. For this reason Landau fluctuations have practically no effect on the energy resolution for this type of detector [9].

In general, the energy resolution of scintillator or liquid-argon sampling calorimeters is superior to that achievable with gaseous detectors. The layers in the liquid-argon sampling calorimeters can be arranged as planar chambers or they can have a more complex shape (*accordion type*). The achieved energy resolution with LAr calorimeters is 8%–10% at 1 GeV [38, 39].

If, as is the case in calorimeters, a sufficient amount of light is available, the light emerging from the end face of a scintillator plate can be absorbed in an external wavelength-shifter rod. This wavelength shifter re-emits the absorbed light isotropically at a larger wavelength and guides it to a photosensitive device (Fig. 8.12).

It is very important that a small air gap remains between the scintillator face and the wavelength-shifter rod. Otherwise, the frequency-shifted, isotropically re-emitted light would not be contained in the wavelength-shifter rod by internal reflection. This method of light transfer normally

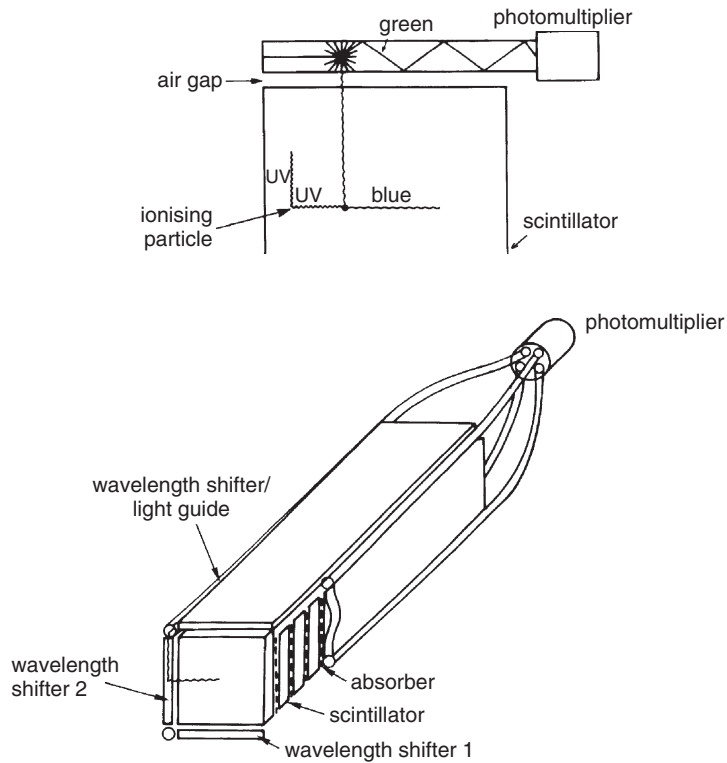


Fig. 8.12. *Wavelength-shifter readout of a scintillator and two-step wavelength-shifter readout of a calorimeter.*

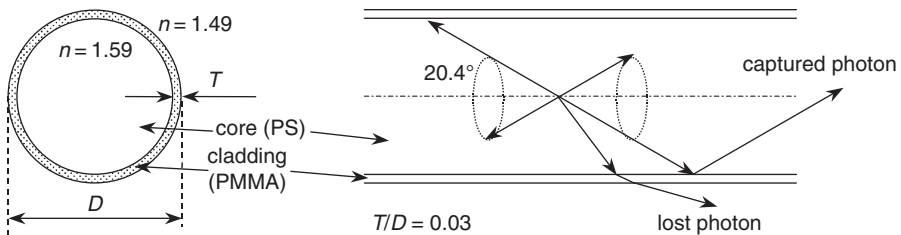


Fig. 8.13. *Structure and principle of operation of the scintillation and light-guiding fibres [40, 41].*

entails an appreciable loss of light; typical conversion values are around 1% to 5%. However, now single- and multicladding scintillation and light-guide fibres are available. The structure and operation principle of such fibres are explained in Fig. 8.13 [40, 41]. The fibres of this type allow light transfer over long distances at small light losses. The fraction of the captured light is typically 3% for single-cladding fibres and up to 6% for

multicladding ones. The cladding-fibre light guides can be glued to the scintillator without any air gap.

A normal sampling calorimeter of absorber plates and scintillator sheets can also be read out by wavelength-shifter rods or fibres running through the scintillator plates perpendicularly [42–44]. The technique of wavelength-shifter readout allows to build rather compact calorimeters.

The scintillation counters used in calorimeters must not necessarily have the form of plates alternating with absorber layers. They can also be embedded as scintillating fibres, for example, in a lead matrix [45, 46]. In this case the readout is greatly simplified because the scintillating fibres can be bent rather strongly without loss of internal reflection. Scintillating fibres can either be read out directly or via light-guide fibres by photomultipliers (*spaghetti calorimeter*). The energy resolution of the scintillation-fibre-based calorimeter of the KLOE detector achieved a value of $\sigma_E/E = 5.7\%/\sqrt{E} [\text{GeV}]$. In addition to high energy resolution, this calorimeter provides precise timing for photons ($\sigma_t \approx 50 \text{ ps}/\sqrt{E} [\text{GeV}]$) due to the short decay time of the light flash of the plastic scintillator [46]. Recently, even a better energy resolution, $4\%/\sqrt{E} [\text{GeV}]$, was reported for a ‘*shashlik*’-type sampling calorimeter developed for the KOPIO experiment [43].

The scintillator readout can also be accomplished by inserting wavelength-shifting fibres into grooves milled into planar scintillator sheets (*tile calorimeter*) [47–49].

8.2 Hadron calorimeters

In principle, *hadron calorimeters* work along the same lines as electron–photon calorimeters, the main difference being that for hadron calorimeters the longitudinal development is determined by the average nuclear interaction length λ_I , which can be roughly estimated as [1]

$$\lambda_I \approx 35 \text{ g/cm}^2 A^{1/3} . \quad (8.35)$$

In most detector materials this is much larger than the radiation length X_0 , which describes the behaviour of electron–photon cascades. This is the reason why hadron calorimeters have to be much larger than electromagnetic shower counters.

Frequently, electron and hadron calorimeters are integrated in a single detector. For example, Fig. 8.14 [50] shows an iron–scintillator calorimeter with separate wavelength-shifter readout for electrons and hadrons. The electron part has a depth of 14 radiation lengths, and the hadron section corresponds to 3.2 interaction lengths.

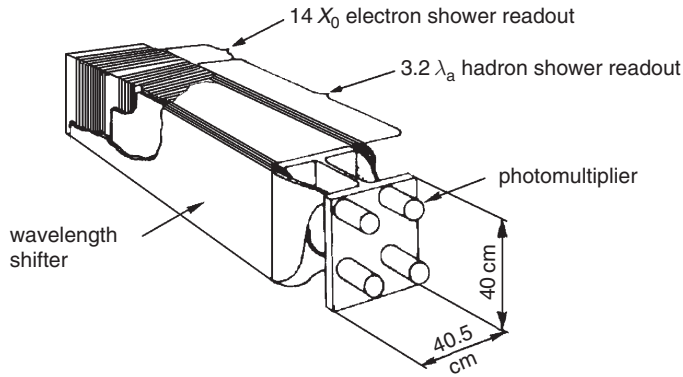


Fig. 8.14. Typical set-up of an iron–scintillator calorimeter with wavelength-shifter readout [50].

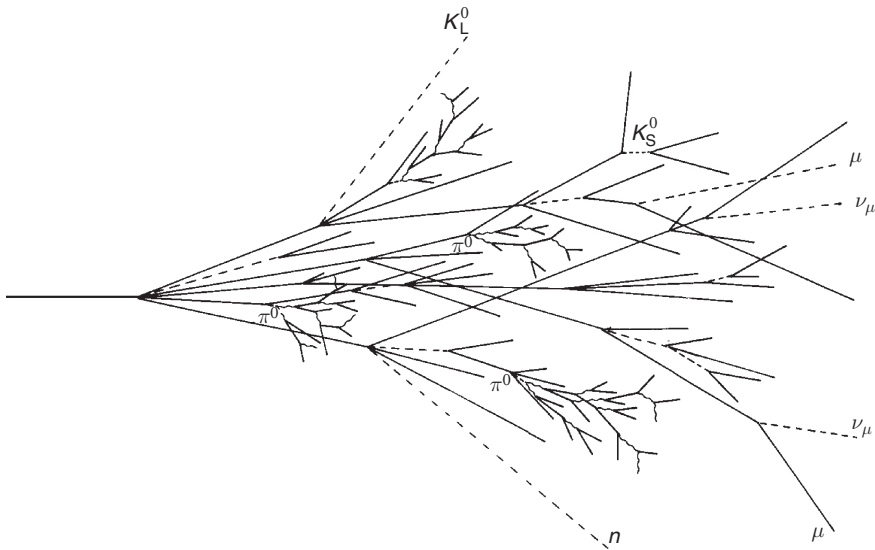


Fig. 8.15. Sketch of a hadron cascade in an absorber.

Apart from the larger *longitudinal development* of hadron cascades, their *lateral width* is also sizably increased compared to electron cascades. While the lateral structure of electron showers is mainly determined by multiple scattering, in hadron cascades it is caused by large transverse momentum transfers in nuclear interactions. Typical processes in a hadron cascade are shown in Fig. 8.15.

Different structures of 250 GeV photon- and proton-induced cascades in the Earth's atmosphere are clearly visible from Fig. 8.16 [51]. The results shown in this case were obtained from a Monte Carlo simulation.

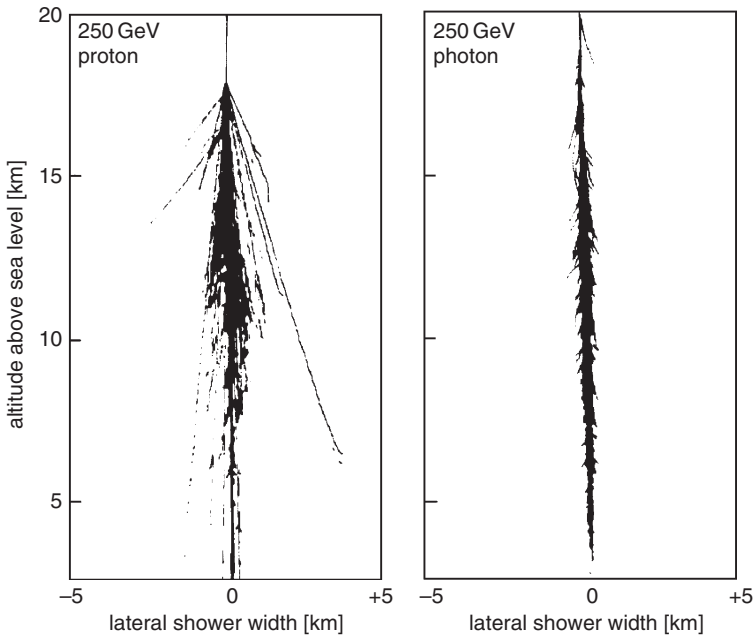


Fig. 8.16. Monte Carlo simulations of the different development of hadronic and electromagnetic cascades in the Earth's atmosphere, induced by 250 GeV protons and photons [51].

The production of secondary particles in a hadron cascade is caused by inelastic hadronic processes. Mainly charged and neutral pions, but, with lower multiplicities, also kaons, nucleons and other hadrons are produced. The average particle multiplicity per interaction varies only weakly with energy ($\propto \ln E$). The average transverse momentum of secondary particles can be characterised by

$$\langle p_T \rangle \approx 0.35 \text{ GeV}/c . \quad (8.36)$$

The average inelasticity, that is, the fraction of energy which is transferred to secondary particles in the interaction, is around 50%.

A large component of the secondary particles in hadron cascades are neutral pions, which represent approximately one third of the pions produced in each inelastic collision. Neutral pions decay rather quickly ($\approx 10^{-16}$ s) into two energetic photons, thereby initiating electromagnetic subcascades in a hadron shower. Therefore, after the first collision 1/3 of the energy is deposited in the form of an electromagnetic shower, at the second stage of multiplication the total fraction of this energy, f_{em} , will be

$$\frac{1}{3} + \left(1 - \frac{1}{3}\right) \frac{1}{3} = 1 - \left(1 - \frac{1}{3}\right)^2, \quad (8.37)$$

and so on. The same argument applies for the leaving hadron. If a hadronic shower comprises n generations, the total electromagnetic fraction is

$$f_{\text{em}} = 1 - \left(1 - \frac{1}{3}\right)^n. \quad (8.38)$$

Assuming that n increases with the energy of the incident hadron we can see that the f_{em} value increases as well.

Of course, this consideration is rather naïve. This effect was analysed in [52] where the following expression was suggested:

$$f_{\text{em}} = 1 - \left(\frac{E}{E_0}\right)^{k-1}, \quad (8.39)$$

where E is the energy of the incident hadron, E_0 is a parameter varying from 0.7 GeV (for iron) to 1.3 GeV (for lead), and k is between 0.8 to 0.85. Details can be found in [11].

π^0 production, however, is subject to large fluctuations, which are determined essentially by the properties of the first inelastic interaction.

Some part of the energy in the hadronic shower is deposited via ionisation losses of the charged hadrons (f_{ion}).

In contrast to electrons and photons, whose electromagnetic energy is almost completely recorded in the detector, a substantial fraction of the energy in hadron cascades remains *invisible* (f_{inv}). This is related to the fact that some part of the hadron energy is used to break up nuclear bonds. This *nuclear binding energy* is provided by the primary and secondary hadrons and does not contribute to the visible energy.

Furthermore, extremely short-range nuclear fragments are produced in the break-up of nuclear bonds. In sampling calorimeters, these fragments do not contribute to the signal since they are absorbed before reaching the detection layers. In addition, long-lived or stable neutral particles like neutrons, K_L^0 , or neutrinos can escape from the calorimeter, thereby reducing the visible energy. Muons created as decay products of pions and kaons deposit in most cases only a very small fraction of their energy in the calorimeter (see the example at the beginning of this chapter). As a result of all these effects, the energy resolution for hadrons is significantly inferior to that of electrons because of the different interaction and particle-production properties. The total *invisible energy fraction* of a hadronic cascade can be estimated as $f_{\text{inv}} \approx 30\%–40\%$ [11].

It is important to remember that only the electromagnetic energy and the energy loss of charged particles can be recorded in a calorimeter.

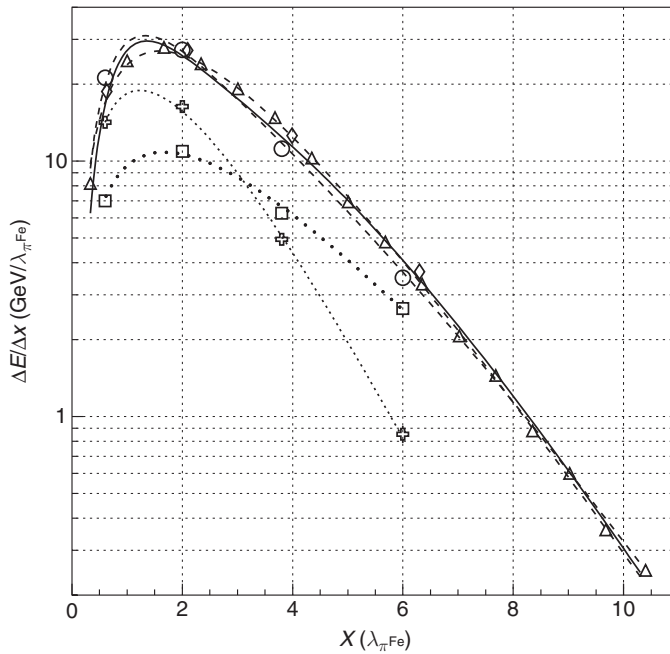


Fig. 8.17. The longitudinal energy distribution in a hadronic shower in iron induced by 100 GeV pions. The depth X is measured in units of the interaction length λ_I . Open circles and triangles are experimental data, diamonds are predictions of a simulation. The dash-dotted line is a simple fit by Formula (8.7) with optimal a and b , the other lines are more sophisticated approximations. Crosses and squares are contributions of electromagnetic showers and the non-electromagnetic part, respectively [53].

Consequently, a hadron signal for the same particle energy is normally smaller than an electron signal.

Figure 8.17 shows the measured longitudinal shower development of 100 GeV pions in iron [53] in comparison to Monte Carlo calculations and empirical approximations. The energy-deposition distributions for a tungsten calorimeter obtained for different pion energies are presented in Fig. 8.18 [54–58]. The lateral shower profiles of 10 GeV/ c pions in iron are shown in Fig. 8.19.

The so-called length of a hadron cascade depends on exactly how this is defined. Regardless of the definition, the length increases with the energy of the incident particle. Figure 8.20 shows the shower lengths and centre of gravity of hadronic cascades for various definitions [55]. One possible definition is given by the requirement that the shower length is reached if, on average, only one particle or less is registered at the depth t . According to this definition a 50 GeV-pion shower in an iron-scintillator calorimeter

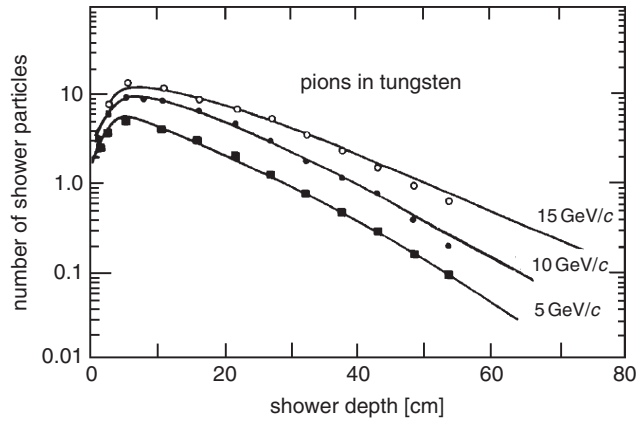


Fig. 8.18. Longitudinal shower development of pions in tungsten [56, 57]. The solid lines are from Monte Carlo simulation [58].

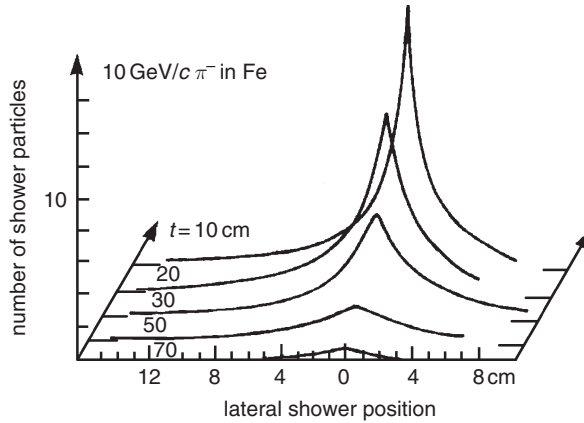


Fig. 8.19. Lateral shower profile of 10 GeV/c pions in iron [59].

is approximately 120 cm Fe ‘long’. An alternative definition is given by the depth before which a certain fraction of the primary energy (e.g. 95%) is contained. A 95% energy containment would lead to a length of 70 cm iron for a 50 GeV-pion shower. The longitudinal centre of gravity of the shower only increases logarithmically with the energy. The position of the centre of gravity of the shower is also shown in Fig. 8.20.

The 95%-longitudinal-containment length in iron can be approximated by [2]

$$L(95\%) = (9.4 \ln(E/\text{GeV}) + 39) \text{ cm} . \tag{8.40}$$

This estimation scaled by the interaction length λ_I characterises the hadronic showers in other materials as well.

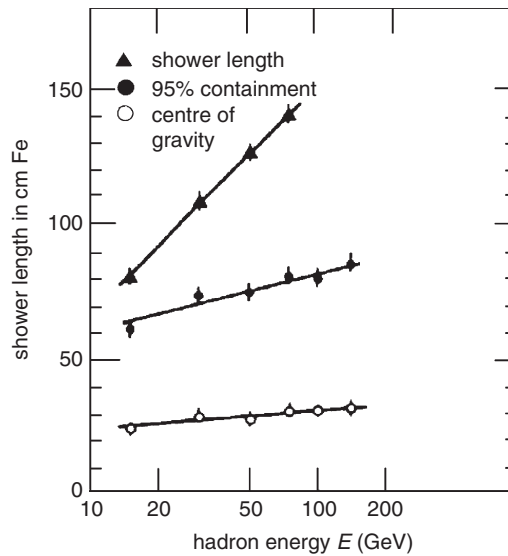


Fig. 8.20. Shower lengths and centre of gravity of hadron cascades for various definitions [55].

Similarly, the *lateral distribution* of cascades can be characterised by a radial width. The lateral distribution of a hadron shower is initially very narrow but becomes wider with increasing calorimeter depth (see Fig. 8.19). The required lateral calorimeter radius for a 95% containment as a function of the longitudinal shower depth is shown in Fig. 8.21 for pions of two different energies in iron [55].

The energy resolution for hadrons is significantly worse compared to electrons because of the large fluctuations in the hadron-shower development. A large contribution to this fact is caused by the difference in the calorimeter response to electrons and hadrons. Due to this difference the fluctuations in the number of neutral pions produced in the hadronic shower create a sizable effect for the energy resolution.

It is, however, possible to regain some part of the ‘invisible’ energy in hadron cascades, thereby equalising the response to electrons and hadrons. This hadron-calorimeter *compensation* is based on the following physical principles [11, 60, 61].

If uranium is used as an absorber material, neutrons will also be produced in nuclear interactions. These neutrons may induce fission of other target nuclei producing more neutrons as well and energetic γ rays as a consequence of nuclear transitions. These neutrons and γ rays can enhance the amplitude of the hadron-shower signal if their energy is recorded. Also for absorber materials other than uranium where fission processes are

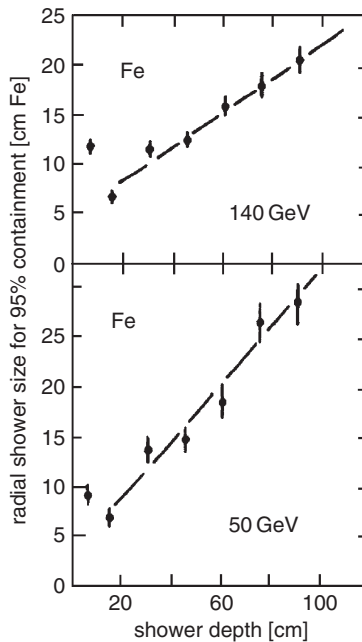


Fig. 8.21. Radius of hadronic showers for 95% containment as a function of the depth in iron [55]. The corresponding total width of the hadron shower is twice the radius.

endotherm, neutrons and γ rays may be produced. The γ rays can contribute to the visible energy by a suitable choice of sampling detectors, and neutrons can produce low-energy recoil protons in (n, p) reactions in detector layers containing hydrogen. These recoil protons also increase the hadron signal.

For energies below 1 GeV even in uranium sampling calorimeters, the lost energy in hadron cascades cannot be regained. By suitable combination (uranium/liquid argon, uranium/copper/scintillator) compensation can be achieved for energies exceeding several GeV. For very high energies (≥ 100 GeV) even *overcompensation* can occur. Such overcompensation can be avoided by limiting the sampling time. Overcompensation can also be caused by a reduction of the electron signal due to saturation effects in the detector layers. Because of the different lateral structure of electron and hadron cascades, saturation effects affect the electron and hadron signals differently.

The best hadron sampling calorimeters (e.g. uranium/scintillator, uranium/liquid argon) reach an energy resolution of [62]

$$\frac{\sigma(E)}{E} = \frac{35\%}{\sqrt{E} [\text{GeV}]} \quad (8.41)$$

However, hadron calorimeters recently developed for the detection of high-energy hadrons at LHC achieved a rather good energy resolution even without compensation. For example, for the ATLAS detector a resolution of about $42\%/\sqrt{E}$ [GeV] was obtained for pions at a total calorimeter thickness of about $8.2 \lambda_I$, and an e/h ratio[†] of about 1.37 was measured [63]. A possible constant term in the parametrisation of the energy resolution usually can safely be neglected for hadronic cascades because the large sampling fluctuations dominate the energy resolution. Only for extremely high energies (≈ 1000 GeV) a constant term will limit the energy resolution.

The energy resolution attainable in hadron calorimeters varies with the number of detector layers (sampling planes) similarly to electromagnetic calorimeters. Experimentally one finds that absorber thicknesses $d < 2$ cm of iron do not lead to an improvement of the energy resolution [2]. Depending on the application as well as on the available financial resources, a large variety of sampling detectors can be considered. Possible candidates for sampling elements in calorimeters are scintillators, liquid-argon or liquid-xenon layers, multiwire proportional chambers, layers of proportional tubes, flash chambers, streamer tubes, Geiger–Müller tubes (with local limitation of the discharge – ‘limited Geiger mode’), parallel-plate chambers and layers of ‘warm’ (i.e. room temperature) liquids (see Chap. 5). Ionisation chambers under high pressure can also be used [64]. For absorber materials, uranium, copper, tungsten and iron are most commonly used, although aluminium and marble calorimeters have also been constructed and operated.

A prominent feature of calorimeters is that their energy resolution $\sigma(E)/E$ improves with increasing energy like $1/\sqrt{E}$, quite in contrast to momentum spectrometers, whose resolution σ_p/p deteriorates linearly with increasing momentum. In addition, calorimeters are rather compact even for high energies, because the shower length only increases logarithmically with the particle energy.

In cosmic-ray experiments involving the energy determination of protons, heavy nuclei and photons of the primary cosmic radiation in the energy range $> 10^{14}$ eV, various calorimetric measurement methods are needed to account for the low particle intensities. Cosmic-ray particles initiate in the Earth’s atmosphere hadronic or electromagnetic cascades (see Fig. 8.16) which can be detected by quite different techniques. The energy of extensive air showers is traditionally determined by sampling their lateral distribution at sea level. This classical method quite obviously suffers from a relatively inaccurate energy determination [65]. Better results are

[†] The e/h ratio is the ratio of energy deposits of an electron-initiated shower compared to that of a hadron-initiated shower for the same initial energy of electrons and hadrons.

obtained if the scintillation or Cherenkov light of the shower particles produced in the atmosphere is recorded (compare Sect. 16.12). To observe the very rare highest-energy cosmic rays, an as large as possible detection volume is necessary. In this case the scintillation of nitrogen produced by the cosmic-ray shower can be detected [66, 67]. Both of these techniques, Cherenkov and air scintillation, however, require – because of the low light yield – clear and moonless nights.

A possible way out or an alternative method is the detection of *geosynchrotron radiation* in the radio band (40–80 MHz) of extensive air showers, which is generated by the deflection of the large number of shower particles in the Earth's magnetic field [68, 69]. It is also conceivable to measure high-energy extensive air showers by *acoustic detection techniques* [70].

An alternative method can be considered for the energy determination of high-energy cosmic neutrinos or muons. These particles easily penetrate the Earth's atmosphere, so that one can also take advantage of the clear and highly transparent water of the ocean, deep lakes or even polar ice as a Cherenkov medium. Muons undergo energy losses at high energies (> 1 TeV) mainly by bremsstrahlung and direct electron-pair production (see Fig. 1.6). These two energy-loss processes are both proportional to the muon energy. A measurement of the energy loss using a three-dimensional matrix of photomultipliers in deep water, shielded from sunlight, allows a determination of the muon energy. Similarly, the energy of electron or muon neutrinos can be roughly determined, if these particles produce electrons or muons in inelastic interactions in water, that, for the case of electrons, induce electromagnetic cascades, and, for the case of muons, they produce a signal proportional to the energy loss. The deep ocean, lake water or polar ice in this case are both interaction targets and detectors for the Cherenkov light produced by the interaction products. Electrons or muons produced in neutrino interactions closely keep the direction of incidence of the neutrinos. Therefore, these deep-water neutrino detectors are at the same time *neutrino telescopes* allowing one to enter the domain of neutrino astronomy in the TeV energy range [71–73].

8.3 Calibration and monitoring of calorimeters

In the modern experiments on particle physics the information is collected as digitised data (see Chap. 15). The pulse height A_i measured in an event from a certain (i th) element of the calorimeter is related to the energy E_i deposited in this element by

$$E_i = \alpha_i(A_i - P_i) , \quad (8.42)$$

where P_i is the pedestal, i.e. the origin of the scale, and α_i is the calibration coefficient. Thus, to keep a good performance of the calorimeter, the following procedures are usually carried out:

- *Pedestal determination* by providing a trigger from a pulser without any signal at the input of the ADC ('random trigger events').
- Electronics channel control by test pulses applied to the input of the electronics chain.
- *Monitoring* of the stability of the calibration coefficients α_i .
- *Absolute energy calibration*, i.e. determination of the α_i values.

In general, the dependence (8.42) can be non-linear. In this case more calibration coefficients are needed to describe the E/A relation.

Prior to real physics experiments a study of the parameters of individual calorimeter elements and modules is usually done in accelerator-test beams which supply identified particles of known momenta. By varying the beam energy the linearity of the calorimeter can be tested and characteristic shower parameters can be recorded. For the calibration of calorimeters designed for low energies, e.g. semiconductor detectors, radioactive sources are normally used. Preferentially used are K-line emitters, like ^{207}Bi , with well-defined monoenergetic electrons or gamma-ray lines, which allow a calibration via the total-absorption peaks.

In addition to energy calibration, the dependence of the calorimeter signal on the point of particle impact, the angle of incidence and the behaviour in magnetic fields is of great importance. In particular, for calorimeters with gas sampling, magnetic-field effects can cause spiralling electrons, which can significantly modify the calibration. In gas sampling calorimeters the particle rate can have influence on the signal amplitude because of dead-time or recovery-time effects. A thorough calibration of a calorimeter therefore requires an extensive knowledge of the various parameter-dependent characteristics.

Big experiments can contain a large number of calorimeter modules, not all of which can be calibrated in test beams. If some of the modules are calibrated in a test beam, the rest can be adjusted relative to them. This relative calibration can be done by using minimum-ionising muons that penetrate many calorimeter modules. In uranium calorimeters, the constant noise caused by the natural radioactivity of the uranium can be used for a relative calibration. If one uses non-radioactive absorber materials in gas sampling calorimeters, a test and relative calibration can also be performed with radioactive noble gases like ^{85}Kr .

Scintillator calorimeters can best be calibrated by feeding defined light signals, e.g. via light-emitting diodes (LEDs), into the detector layers and recording the output signals from the photomultipliers. To avoid variations in the injected light intensity, which may be caused by different light yields of the individual light diodes, a single light source can be used (e.g. a laser), which distributes its light via a manifold of light fibres to the scintillation counters [2].

Once a complex calorimeter system has been calibrated, one has to ensure that the calibration constants do not vary or, if they do, the drift of the calibration parameters must be monitored. The time stability of the calibration can be checked with, e.g., cosmic-ray muons. In some cases some calorimeter modules may be positioned unfavourably so that the rate of cosmic-ray muons is insufficient for accurate stability control. Therefore, reference measurements have to be performed periodically by injecting calibrated reference signals into the various detector layers or into the inputs of the readout electronics. The calibration and monitoring of scintillation crystal calorimeters can be performed using cosmic-ray muons as it was demonstrated in [74, 75].

In gas sampling calorimeters the output signal can in principle only vary because of a change of gas parameters and high voltage. In this case, a test chamber supplied with the detector gas can be used for monitoring. To do that, the current, the pulse rate or the spectrum under the exposition to characteristic X rays of a radioactive source should be continuously measured. A change in the measured X-ray energy in this test chamber indicates a time-dependent calibration which can be compensated by an adjustment of the high voltage.

In some experiments there are always particles that can be used for calibration and monitoring. For example, elastic Bhabha scattering ($e^+e^- \rightarrow e^+e^-$) can be used to calibrate the electromagnetic calorimeters in an e^+e^- scattering experiment, since the final-state particles – if one neglects radiative effects – have known beam energy. In the same way, the reaction $e^+e^- \rightarrow q\bar{q}$ (e.g. going through a resonance of known mass, like m_Z , if one wants to be independent of initial-state radiation) with subsequent hadronisation of the quarks can be used to check the performance of a hadron calorimeter. Finally, muon-pair production ($e^+e^- \rightarrow \mu^+\mu^-$) supplies final-state muons with known momentum (= beam momentum at high energies), which can reach all detector modules because of their nearly flat angular distribution ($d\sigma/d\Omega \propto 1 + \cos^2\theta$, where θ is the angle between e^- and μ^-).

It should be noted that the energy of an electron or hadron absorbed in the calorimeter is distributed over a cluster of crystals. The total deposited energy can be expressed as a sum

$$E = \sum_{i=1}^M \alpha_i A_i , \quad (8.43)$$

where pedestals are assumed to be already subtracted. Then, the calibration coefficients are determined by minimisation of the functional

$$L = \sum_{k=1}^N \left(\sum_{i=1}^M \alpha_i A_{ik} - E_{0k} \right)^2 , \quad (8.44)$$

where the first summation is performed over all N events selected for calibration, A_{ik} is the response of the i th calorimeter element in the k th event and E_{0k} is the known incident particle energy in the k th event. Requiring for all α_j

$$\frac{\partial L}{\partial \alpha_j} = 0 , \quad (8.45)$$

we obtain a linear equation system for the determination of the calibration constants,

$$\sum_{i=1}^M \alpha_i \left(\sum_{k=1}^N A_{jk} A_{ik} \right) = \sum_{k=1}^N E_{0k} A_{jk} . \quad (8.46)$$

8.4 Cryogenic calorimeters

The calorimeters described so far can be used for the spectroscopy of particles from the MeV range up to the highest energies. For many investigations the detection of particles of extremely low energy in the range between 1 eV and 1000 eV is of great interest. Calorimeters for such low-energy particles are used for the detection of and search for low-energy cosmic neutrinos, weakly interacting massive particles (WIMPs) or other candidates of dark, non-luminous matter, X-ray spectroscopy for astrophysics and material science, single-optical-photon spectroscopy and in other experiments [76–79]. In the past 20 years this field of experimental particle physics has developed intensively and by now it comprises dozens of projects [80, 81].

To reduce the detection threshold and improve at the same time the calorimeter energy resolution, it is only natural to replace the ionisation or electron–hole pair production by *quantum transitions* requiring lower energies (see Sect. 5.3).

Phonons in solid-state materials have energies around 10^{-5} eV for temperatures around 100 mK. The other types of quasiparticles at low temperature are *Cooper pairs* in a superconductor which are bound states

of two electrons with opposite spin that behave like bosons and will form at sufficiently low temperatures a Bose condensate. Cooper pairs in superconductors have binding energies in the range between $4 \cdot 10^{-5}$ eV (Ir) and $3 \cdot 10^{-3}$ eV (Nb). Thus, even extremely low energy depositions would produce a large number of phonons or break up Cooper pairs. To avoid thermal excitations of these quantum processes, such calorimeters, however, would have to be operated at extremely low temperatures, typically in the milli-Kelvin range. For this reason, such calorimeters are called *cryogenic detectors*. Cryogenic calorimeters can be subdivided in two main categories: first, detectors for quasiparticles in superconducting materials or suitable crystals, and secondly, phonon detectors in insulators.

One detection method is based on the fact that the superconductivity of a substance is destroyed by energy deposition if the detector element is sufficiently small. This is the working principle of superheated superconducting granules [82]. In this case the cryogenic calorimeter is made of a large number of superconducting spheres with diameters in the micrometre range. If these granules are embedded in a magnetic field, and the energy deposition of a low-energy particle transfers one particular granule from the superconducting to the normal-conducting state, this transition can be detected by the suppression of the *Meissner effect*. This is where the magnetic field, which does not enter the granule in the superconducting state, now again passes through the normal-conducting granule. The transition from the superconducting to the normal-conducting state can be detected by pickup coils coupled to very sensitive preamplifiers or by SQUIDS (*Superconducting Quantum Interference Devices*) [83]. These *quantum interferometers* are extremely sensitive detection devices for magnetic effects. The operation principle of a SQUID is based on the *Josephson effect*, which represents a tunnel effect operating between two superconductors separated by thin insulating layers. In contrast to the normal one-particle tunnel effect, known, e.g. from α decay, the Josephson effect involves the tunnelling of Cooper pairs. In Josephson junctions, interference effects of the tunnel current occur which can be influenced by magnetic fields. The structure of these interference effects is related to the size of the magnetic flux quanta [84–86].

An alternative method to detect *quasiparticles* is to let them directly tunnel through an insulating foil between two superconductors (SIS – Superconducting–Insulating–Superconducting transition) [87]. In this case the problem arises of keeping undesired leakage currents at an extremely low level.

In contrast to Cooper pairs, phonons, which can be excited by energy depositions in insulators, can be detected with methods of classical calorimetry. If ΔE is the absorbed energy, this results in a temperature rise of

$$\Delta T = \Delta E / mc , \quad (8.47)$$

where c is the specific heat capacity and m the mass of the calorimeter. If these calorimetric measurements are performed at very low temperatures, where c can be very small (the lattice contribution to the specific heat is proportional to T^3 at low temperatures), this method is also used to detect individual particles. In a real experiment, the temperature change is recorded with a thermistor, which is basically an NTC resistor (negative temperature coefficient), embedded into or fixed to an ultrapure crystal. The crystal represents the absorber, i.e. the detector for the radiation that is to be measured. Because of the discrete energy of phonons, one would expect discontinuous thermal energy fluctuations which can be detected with electronic filter techniques.

In Fig. 8.22 the principle of such a calorimeter is sketched [88].

In this way α particles and γ rays have been detected in a large TeO_2 crystal at 15 mK in a purely thermal detector with thermistor readout with an energy resolution of 4.2 keV FWHM for 5.4 MeV α particles [89]. Special bolometers have also been developed in which heat and ionisation signals are measured simultaneously [90, 91].

Thermal detectors provide promise for improvements of energy resolutions. For example, a 1 mm cubic crystal of silicon kept at 20 mK would have a heat capacity of $5 \cdot 10^{-15}$ J/K and a FWHM energy resolution of 0.1 eV (corresponding to $\sigma = 42$ meV) [92].

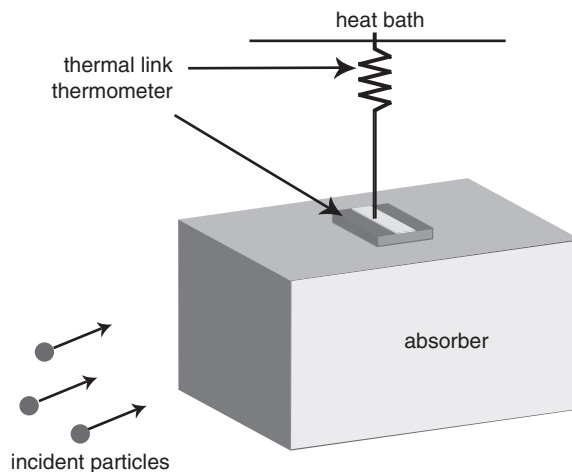


Fig. 8.22. Schematic of a cryogenic calorimeter. The basic components are the absorber for incident particles, a thermometer for detecting the heat signal and a thermal link to the heat bath [88].

Joint efforts in the fields of cryogenics, particle physics and astrophysics are required, which may lead to exciting and unexpected results. One interesting goal would be to detect relic neutrinos of the Big Bang with energies around $200 \mu\text{eV}$ [92].

At present cryogenic calorimeters are most frequently used in the search for *weakly interacting massive particles* (WIMPs). The interaction cross section for WIMP interactions is extremely small, so that possible backgrounds have to be reduced to a very low level. Unfortunately, also the energy transfer of a WIMP to a target nucleus in a cryogenic detector is only in the range of $\approx 10 \text{ keV}$. An excellent method to discriminate a WIMP signal against the background caused, e.g., by local radioactivity is to use scintillating crystals like CaWO_4 , CdWO_4 or ZnWO_4 . These scintillators allow to measure the light yield at low temperatures and the phonon production by WIMP interactions at the same time. *Nuclear recoils* due to WIMP–nucleon scattering produce mainly phonons and very little scintillation light, while in *electron recoils* also a substantial amount of scintillation light is created. A schematic view of such a cryogenic detector system is shown in Fig. 8.23 [88].

Particles are absorbed in a scintillating dielectric crystal. The scintillation light is detected in a silicon wafer while the phonons are measured in two tungsten thermometers, one of which can be coupled to the silicon detector to increase the sensitivity of the detector. The whole detector

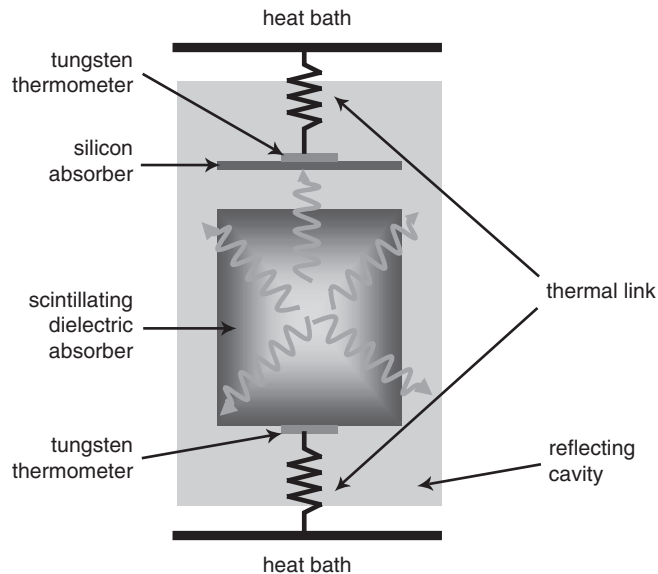


Fig. 8.23. Schematic view of a cryogenic detector with coincident phonon and light detection [88].

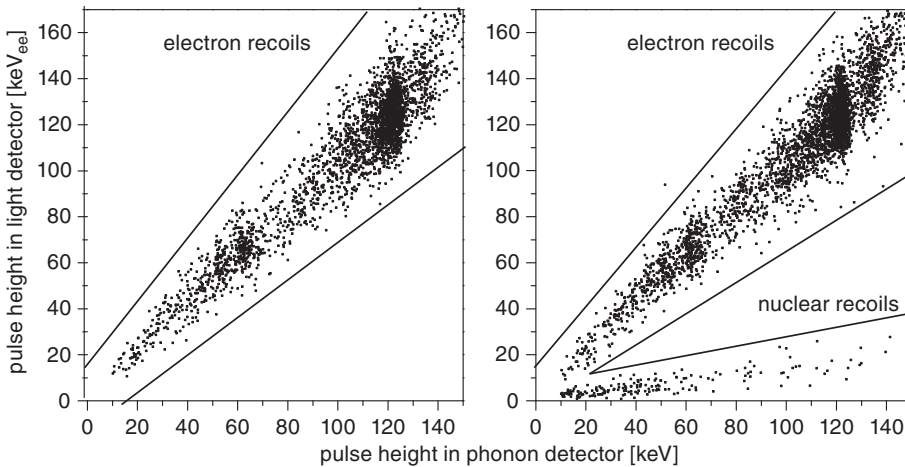


Fig. 8.24. Scatter plot of the pulse height in the light detector from photons of the CaWO_4 crystal versus the pulse height from phonons from the same crystal. The left-hand part of the figure shows the response of the detector to photons and electrons only, while in the right-hand part also neutron interactions are included. The purpose of the lines is just to guide the eye [88, 93].

setup is enclosed in a reflecting cavity and operated at milli-Kelvin temperatures.

The response of a CaWO_4 cryogenic calorimeter to electron recoils and nuclear recoils is shown in Fig. 8.24 [88, 93].

Electron recoils were created by irradiating the crystal with 122 keV and 136 keV photons from a ^{57}Co source and electrons from a ^{90}Sr β source (left panel). To simulate also WIMP interactions the detector was bombarded with neutrons from an americium–beryllium source leading to phonon and scintillation-light yields as shown in the right-hand plot of Fig. 8.24. The light output due to electron recoils caused by photons or electrons (which constitute the main background for WIMP searches) is quite high, whereas nuclear recoils created by neutrons provide a strong phonon signal with only low light yield. It is conjectured that WIMP interactions will look similar to neutron scattering, thus allowing a substantial background rejection if appropriate cuts in the scatter diagram of light versus phonon yield are applied. However, the figure also shows that the suppression of electron recoils at energies below 20 keV becomes rather difficult.

The set-up of a cryogenic detector, based on the energy absorption in *superheated superconducting granules*, is shown in Fig. 8.25 [94]. The system of granules and pickup coil was rotatable by 360° around an axis perpendicular to the magnetic field. This was used to investigate the dependence of the critical field strength for reaching the superconducting

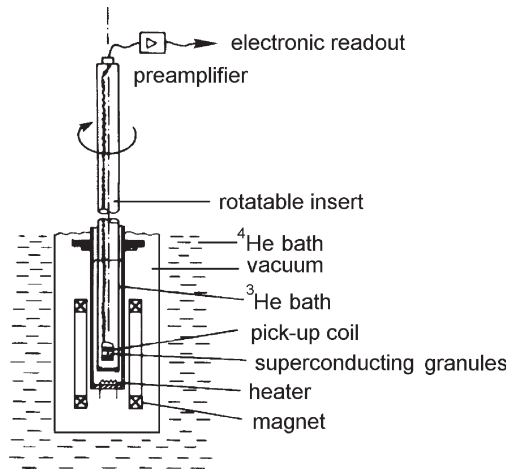


Fig. 8.25. Experimental set-up of a cryogenic detector based on superheated superconducting granules (SSG) [94].

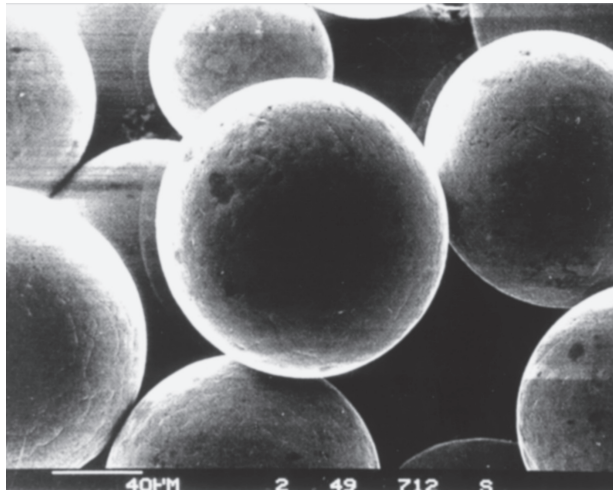


Fig. 8.26. Tin granules (diameter = 130 μm) as a cryogenic calorimeter. A small energy absorption can warm the granules by an amount sufficient to cause a change from the superconducting state to the normal-conducting state, thereby providing a detectable signal [82].

state on the orientation of the granules with respect to the magnetic field. This system succeeded in detecting quantum transitions in tin, zinc and aluminium granules at ^4He and ^3He temperatures. Figure 8.26 shows a microphotograph of tin granules [82, 95]. At present it is already possible to manufacture tin granules with diameters as small as 5 μm .

With a detector consisting of superheated superconducting granules, it has already been shown that one can detect minimum-ionising particles unambiguously [95].

The detection of transitions from the superconducting into the normal-conducting state with signal amplitudes of about $100\mu\text{V}$ and recovery times of 10 ns to 50 ns already indicates that *superconducting strip counters* are possible candidates for microvertex detectors for future generations of particle physics experiments [96].

8.5 Problems

- 8.1** In an experiment an η meson with total energy $E_0 = 2000\text{ MeV}$ is produced in the laboratory frame. Estimate the width of the η mass peak measured in a calorimeter which has an energy and angular resolution of $\sigma_E/E = 5\%$ and $\sigma_\theta = 0.05$ radian, respectively ($m_\eta = 547.51\text{ MeV}$).
- 8.2** Photons of 1 GeV (100 MeV) energy are detected in a NaI(Tl) calorimeter which has an energy resolution $\sigma_E/E = 1.5\%/(E [\text{GeV}])^{1/4}$. Determine how the pulse-height distribution would change if an aluminium sheet of $L = 0.5 X_0$ thickness would be placed in front of the calorimeter. Estimate the resulting decrease of the energy resolution.
- 8.3** Estimate the quality of a pion/electron separation for a total particle energy of $E = 500\text{ MeV}$ using the energy deposition in a calorimeter based on NaI(Tl) crystals of $15 X_0$ length. For the estimation assume that the main mixing effect consists of pion charge exchange on nuclei which occurs with 50% probability when the pion interacts with nuclei. In this charge-exchange reaction the charged pion is transformed into a neutral pion which initiates an electromagnetic cascade.

References

- [1] Particle Data Group, Review of Particle Physics, S. Eidelman *et al.*, *Phys. Lett.* **B592** Vol. 1–4 (2004) 1–1109; W.-M. Yao *et al.*, *J. Phys.* **G33** (2006) 1–1232; <http://pdg.lbl.gov>
- [2] K. Kleinknecht, *Detektoren für Teilchenstrahlung*, Teubner, Stuttgart (1984, 1987, 1992); *Detectors for Particle Radiation*, Cambridge University Press, Cambridge (1986)

- [3] O.C. Allkofer & C. Grupen, Introduction II: Cosmic Rays in the Atmosphere, in A. Bruzek & H. Pilkuhn (eds.), *Lectures on Space Physics 1*, Bertelsmann Universitätsverlag, Gütersloh (1973) 35–54
- [4] O.F. Nemets & Yu.V. Gofman, *Spravochnik po yadernoi fizike*, Naukova dumka, Kiev (1975)
- [5] B. Rossi, *High Energy Particles*, Prentice-Hall, Englewood Cliffs (1952)
- [6] W.R. Nelson *et al.*, *The EGS4 Code System*, SLAC-R-265 (1985)
- [7] E. Longo & I. Sestili, Monte Carlo Calculation of Photon-Initiated Electromagnetic Showers in Lead Glass, *Nucl. Instr. Meth.* **128** (1975) 283–307; Erratum, *ibid.*, **135** (1976) 587–90
- [8] R. Baumgart, *Messung und Modellierung von Elektron- und Hadron-Kaskaden in Streamerrohrkalorimetern*, Ph.D. Thesis, University of Siegen (1987)
- [9] R. Baumgart *et al.*, Performance Characteristics of an Electromagnetic Streamer Tube Calorimeter, *Nucl. Instr. Meth.* **A256** (1987) 254–60
- [10] N. Akchurin *et al.*, Electromagnetic Shower Profile Measurements in Iron with 500 MeV Electrons, *Nucl. Instr. Meth.* **A471** (2001) 303–13
- [11] R. Wigmans, *Calorimetry: Energy Measurement in Particle Physics*, Clarendon Press, Oxford (2000)
- [12] S. Iwata, *Calorimeters*, Nagoya University Preprint DPNU-13-80 (1980)
- [13] S. Iwata, *Calorimeters (Total Absorption Detectors) for High Energy Experiments at Accelerators*, Nagoya University Preprint DPNU-3-79 (1979)
- [14] L.D. Landau, *The Collected Papers of L.D. Landau*, Pergamon Press, London (1965); A.B. Migdal, Bremsstrahlung and Pair Production in Condensed Media at High Energies, *Phys. Rev.* **103** (1956) 1811–20
- [15] E. Konishi *et al.*, *Three Dimensional Cascade Showers in Lead Taking Account of the Landau-Pomeranchuk-Migdal Effect*, Inst. for Cosmic Rays, Tokyo, ICR Report 36-76-3 (1976)
- [16] *Photon Theory Verified after 40 Years*, CERN-Courier **34(1)** (1994) 12–13
- [17] R. Becker-Szendy *et al.* (SLAC-E-146 Collaboration), *Quantummechanical Suppression of Bremsstrahlung*, SLAC-Pub-6400 (1993)
- [18] M. Oreglia *et al.*, Study of the Reaction $\psi' \rightarrow \gamma\gamma J/\psi$, *Phys. Rev.* **D25** (1982) 2259–77
- [19] E. Blucher *et al.*, Tests of Cesium Iodide Crystals for Electromagnetic Calorimeter, *Nucl. Instr. Meth.* **A249** (1986) 201–27
- [20] B. Aubert, The BaBar Detector, *Nucl. Instr. Meth.* **A479** (2002) 1–116; B. Lewandowski, The BaBar Electromagnetic Calorimeter, *Nucl. Instr. Meth.* **A494** (2002) 303–7
- [21] A. Abashian *et al.* (Belle collaboration), The Belle Detector, *Nucl. Instr. Meth.* **A479** (2002) 117–232
- [22] P.N. Shanahan, *The Performance of a New CsI Calorimeter for the KTeV Experiment at Fermilab*, Proc. of the Sixth Int. Conf. on Calorimetry in High Energy Physics, Frascati, 8–14 June 1996, printed in Frascati Physics Series, Vol. VI, Frascati (1996); V. Prasad, Performance of the Cesium Iodide Calorimeter at the KTeV Experiment at Fermilab, *Nucl. Instr. Meth.* **A461** (2001) 341–3

- [23] B.A. Shwartz, *Performance and Upgrade Plans of the Belle Calorimeter*, Proc. of the 10th Int. Conf. on Calorimetry in Particle Physics, Pasadena, 25–29 March 2002, 182–6
- [24] H. Ikeda *et al.*, A Detailed Test of the CsI(Tl) Calorimeter for Belle with Photon Beams of Energy between 20 MeV and 5.4 GeV, *Nucl. Instr. Meth.* **A441** (2000) 401–26
- [25] *The Compact Muon Solenoid Technical Proposal*, CERN/LHCC **94-38** (1994)
- [26] *9. CMS ECAL Technical Design Report*, CERN/LHCC **97-33** (1997)
- [27] K. Deiters *et al.*, Properties of the Avalanche Photodiodes for the CMS Electromagnetic Calorimeter, *Nucl. Instr. Meth.* **A453** (2000) 223–6
- [28] A. Ghezzi, Recent Testbeam Results of the CMS Electromagnetic Calorimeter, *Nucl. Phys. B Proc. Suppl.* **B150** (2006) 93–7
- [29] <http://opal.web.cern.ch/Opal/>
- [30] SELEX collaboration (M.Y. Balatz *et al.*), *The Lead-Glass Electromagnetic Calorimeter for the SELEX Experiment*, FERMILAB-TM-2252 (July 2004) 42pp.; *Nucl. Instr. Meth.* **A545** (2005) 114–38
- [31] T. Doke, A Historical View on the R&D for Liquid Rare Gas Detectors, *Nucl. Instr. Meth.* **A327** (1993) 113–18
- [32] A.A. Grebenuk, Liquid Noble Gas Calorimeters for KEDR and CMD-2M Detectors, *Nucl. Instr. Meth.* **A453** (2000) 199–204
- [33] M. Jeitler, The NA48 Liquid-Krypton Calorimeter, *Nucl. Instr. Meth.* **A494** (2002) 373–7
- [34] V.M. Aulchenko *et al.*, Investigation of Electromagnetic Calorimeter Based on Liquid Krypton, *Nucl. Instr. Meth.* **A289** (1990) 468–74
- [35] V.M. Aulchenko *et al.*, The Test of the LKR Calorimeter Prototype at the Tagged Photon Beam, *Nucl. Instr. Meth.* **A394** (1997) 35–45
- [36] U. Amaldi, Fluctuations in Calorimetric Measurements, *Phys. Scripta* **23** (1981) 409–24
- [37] C.W. Fabjan, Calorimetry in High Energy Physics, in T. Ferbel (ed.), *Proceedings on Techniques and Concepts of High Energy Physics*, Plenum, New York (1985) 281; CERN-EP-85-54 (1985)
- [38] D. Axen *et al.*, The Lead-Liquid Argon Sampling Calorimeter of the SLD Detector, *Nucl. Instr. Meth.* **A328** (1993) 472–94
- [39] B. Aubert *et al.*, Construction, Assembly and Tests of the ATLAS Electromagnetic Barrel Calorimeter, *Nucl. Instr. Meth.* **A558** (2006) 388–93
- [40] Scintillation materials, Catalogue, Kuraray Co. Ltd. (2000)
- [41] Scintillation products, Scintillating optical fibers, Saint-Gobain brochure, Saint-gobain ceramics & plastics Inc. (2005)
- [42] F. Barreiro *et al.*, An Electromagnetic Calorimeter with Scintillator Strips and Wavelength Shifter Read Out, *Nucl. Instr. Meth.* **A257** (1987) 145–54
- [43] G.S. Atoian *et al.*, Development of Shashlyk Calorimeter for KOPIO, *Nucl. Instr. Meth.* **A531** (2004) 467–80
- [44] The LHCb Collaboration, LHCb Calorimeters (Technical Design Report), CERN/LHCC 2000-0036, LHCb TDR 2 (2000) CERN, Geneve

- [45] D. Acosta *et al.*, Lateral Shower Profiles in a Lead Scintillating-Fiber Calorimeter, *Nucl. Instr. Meth.* **A316** (1992) 184–201
- [46] M. Adinolfi *et al.*, The KLOE Electromagnetic Calorimeter, *Nucl. Instr. Meth.* **A482** (2002) 364–86
- [47] Y. Fujii, *Design Optimisation, Simulation, and Bench Test of a Fine-Granularity Tile/Fiber EM Calorimeter Test Module*, International Workshop on Linear Colliders (LCWS 2002), Jeju Island, Korea, 26–30 August 2002; published in ‘Seogwipo 2002, Linear colliders’ 588–91
- [48] K. Hara *et al.*, Design of a 2×2 Scintillating Tile Calorimeter Package for the SDC Barrel Electromagnetic Tile/Fiber Calorimeter, *Nucl. Instr. Meth.* **A373** (1996) 347–57
- [49] S. Aota *et al.*, A Scintillating Tile/Fiber System for the CDF Upgrade em Calorimeter, *Nucl. Instr. Meth.* **A352** (1995) 557–68
- [50] B.M. Bleichert *et al.*, The Response of a Simple Modular Electron/Hadron Calorimeter to Electrons, *Nucl. Instr. Meth.* **199** (1982) 461–4
- [51] T.C. Weekes, Very High Energy Gamma-Ray Astronomy, *Phys. Rep.* **160** (1988) 1–121
- [52] T.A. Gabriel *et al.*, Energy Dependence of Hadronic Activity, *Nucl. Instr. Meth.* **A338** (1994) 336–47
- [53] P. Amaral *et al.*, Hadronic Shower Development in Iron-Scintillator Tile Calorimetry, *Nucl. Instr. Meth.* **A443** (2000) 51–70
- [54] M. Holder *et al.*, A Detector for High Energy Neutrino Interactions, *Nucl. Instr. Meth.* **148** (1978) 235–49
- [55] M. Holder *et al.*, Performance of a Magnetized Total Absorption Calorimeter Between 15 GeV and 140 GeV, *Nucl. Instr. Meth.* **151** (1978) 69–80
- [56] D.L. Cheshire *et al.*, Measurements on the Development of Cascades in a Tungsten-Scintillator Ionization Spectrometer, *Nucl. Instr. Meth.* **126** (1975) 253–62
- [57] D.L. Cheshire *et al.*, Inelastic Interaction Mean Free Path of Negative Pions in Tungsten, *Phys. Rev.* **D12** (1975) 2587–93
- [58] A. Grant, A Monte Carlo Calculation of High Energy Hadronic Cascades in Iron, *Nucl. Instr. Meth.* **131** (1975) 167–72
- [59] B. Friend *et al.*, Measurements of Energy Flow Distributions of 10 GeV/c Hadronic Showers in Iron and Aluminium, *Nucl. Instr. Meth.* **136** (1976) 505–10
- [60] R. Wigmans, *Advances in Hadron Calorimetry*, CERN-PPE-91-39 (1991)
- [61] C. Leroy & P. Rancoita, Physics of Cascading Shower Generation and Propagation in Matter: Principles of High-Energy, Ultrahigh-Energy and Compensating Calorimetry, *Rep. Prog. Phys.* **63** (2000) 505–606
- [62] A. Bernstein *et al.*, Beam Tests of the ZEUS Barrel Calorimeter, *Nucl. Instr. Meth.* **336** (1993) 23–52
- [63] P. Puso *et al.*, ATLAS Calorimetry, *Nucl. Instr. Meth.* **A494** (2002) 340–5
- [64] S. Denisov *et al.*, A Fine Grain Gas Ionization Calorimeter, *Nucl. Instr. Meth.* **A335** (1993) 106–12

- [65] P. Baillon, *Detection of Atmospheric Cascades at Ground Level*, CERN-PPE-91-012 (1991)
- [66] M. Kleifges and the Auger Collaboration, Status of the Southern Pierre Auger Observatory, *Nucl. Phys. B Proc. Suppl.* **150** (2006) 181–5
- [67] High Resolution Fly’s Eye: <http://hires.physics.utah.edu/>; www.telescopearray.org/
- [68] H. Falcke *et al.*, LOPES Collaboration, Detection and Imaging of Atmospheric Radio Flashes from Cosmic Ray Air Showers, *Nature* **435** (2005) 313–16
- [69] C. Grupen *et al.*, Radio Detection of Cosmic Rays with LOPES, *Braz. J. Phys.* **36(4A)** (2006) 1157–64
- [70] X. Gao, Y. Liu & S. Du, *Acoustic Detection of Air Shower Cores*, 19th Intern. Cosmic Ray Conf., Vol. 8 (1985) 333–6
- [71] S. Barwick *et al.*, Neutrino Astronomy on the 1 km² Scale, *J. Phys.* **G18** (1992) 225–47
- [72] Y. Totsuka, Neutrino Astronomy, *Rep. Progr. Phys.* **55(3)** (1992) 377–430
- [73] Chr. Spiering, Neutrinoastronomie mit Unterwasserteleskopen, *Phys. Bl.* **49(10)** (1993) 871–5
- [74] M.N. Achasov *et al.*, Energy Calibration of the NaI(Tl) Calorimeter of the SND Detector Using Cosmic Muons, *Nucl. Instr. Meth.* **A401** (1997) 179–86
- [75] E. Erlez *et al.*, Cosmic Muon Tomography of Pure Cesium Iodide Calorimeter Crystals, *Nucl. Instr. Meth.* **A440** (2000) 57–85
- [76] K. Pretzl, Cryogenic Calorimeters in Astro and Particle Physics, *Nucl. Instr. Meth.* **A454** (2000) 114–27
- [77] E. Previtali, 20 years of Cryogenic Particle Detectors: Past, Present and Future, *Nucl. Phys. B Proc. Suppl.* **A150** (2006) 3–8
- [78] E. Fiorini, Introduction or ‘Low-Temperature Detectors: Yesterday, Today and Tomorrow’, *Nucl. Instr. Meth.* **A520** (2004) 1–3
- [79] A. Nucciotti, Application of Cryogenic Detectors in Subnuclear and Astroparticle Physics, *Nucl. Instr. Meth.* **A559** (2006) 334–6
- [80] T.O. Niinikoski, Early Developments and Future Directions in LTDs, *Nucl. Instr. Meth.* **A559** (2006) 330–3
- [81] G. Waysand, A Modest Prehistory of Low-Temperature Detectors, *Nucl. Instr. Meth.* **520** (2004) 4–10
- [82] K.P. Pretzl, Superconducting Granule Detectors, *Particle World* **1** (1990) 153–62
- [83] V.N. Trofimov, *SQUIDS in Thermal Detectors of Weakly Interacting Particles*, Dubna-Preprint E8-91-67 (1991)
- [84] C. Kittel, *Introduction to Solid State Physics*, 8th edition, Wiley Interscience, New York (2005); *Einführung in die Festkörperphysik*, Oldenbourg, München/Wien (1980)
- [85] N.W. Ashcroft & N.D. Mermin, *Solid State Physics*, Holt-Saunders, New York (1976)
- [86] K.H. Hellwege, *Einführung in die Festkörperphysik*, Springer, Berlin/Heidelberg/New York (1976)

- [87] J.R. Primack, D. Seckel & B. Sadoulet, Detection of Cosmic Dark Matter, *Ann. Rev. Nucl. Part. Sci.* **38** (1988) 751–807
- [88] I. Bavykina, *Investigation of ZnWO₄ Crystals as an Absorber in the CRESST Dark Matter Search*, Master Thesis, University of Siegen (March 2006)
- [89] A. Alessandrello, A Massive Thermal Detector for Alpha and Gamma Spectroscopy, *Nucl. Instr. Meth.* **A440** (2000) 397–402
- [90] D. Yvon *et al.*, *Bolometer Development, with Simultaneous Measurement of Heat and Ionization Signals*, Saclay-Preprint CEN-DAPNIA-SPP 93-11 (1993)
- [91] F. Petricca *et al.*, CRESST: First Results with the Phonon-Light Technique, *Nucl. Instr. Meth.* **A559** (2006) 375–7
- [92] E. Fiorini, Underground Cryogenic Detectors, *Europhys. News* **23** (1992) 207–9
- [93] P. Meunier *et al.*, Discrimination between Nuclear Recoils and Electron Recoils by Simultaneous Detection of Phonons and Scintillation Light, *Appl. Phys. Lett.* **75(9)** (1999) 1335–7
- [94] M. Frank *et al.*, Study of Single Superconducting Grains for a Neutrino and Dark Matter Detector, *Nucl. Instr. Meth.* **A287** (1990) 583–94
- [95] S. Janos *et al.*, The Bern Cryogenic Detector System for Dark Matter Search, *Nucl. Instr. Meth.* **A547** (2005) 359–67
- [96] A. Gabutti *et al.*, A Fast, Self-Recovering Superconducting Strip Particle Detector Made with Granular Tungsten, *Nucl. Instr. Meth.* **A312** (1992) 475–82